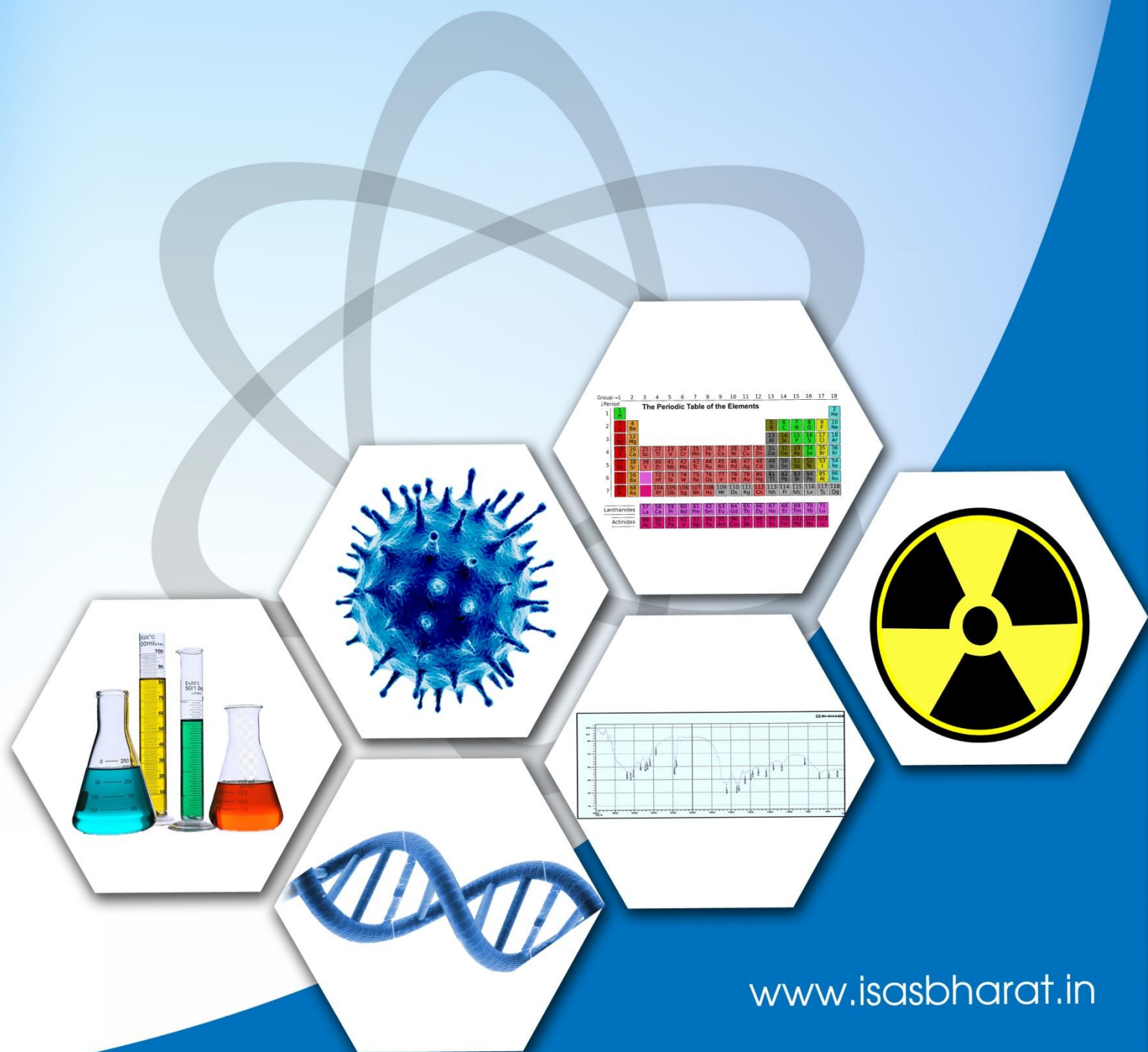




ISSN:2583-5459
Volume 2 Issue 2
October, 2023

Journal of ISAS

An open access peer reviewed quarterly e-journal by
Indian Society of Analytical Scientists





Journal of ISAS

An open access peer reviewed quarterly e-journal published by Indian Society of Analytical Scientists

Published by: Indian Society of Analytical Scientists (ISAS)

Address: C/o REDS, BARC, Mumbai 400085

Email: isasjournal@isasbharat.in

President ISAS: Dr. Raghaw Saran

J. ISAS

Editorial Board

Editor in Chief

Dr. Nilima Rajurkar, Pune

Members

Dr. Vijayalaxmi C. Adya, Mumbai

Dr. A. K. Basu, Pune

Dr. Vinay Bhandari, Pune

Dr. Avinash Bharati, Nagpur

Dr. Anu Gopinath, Kochi

Dr. Ravin Jugade, Nagpur

Dr. Padmaja S. Vadodara

Dr. Pradeep Kumar, Mumbai

Dr. Prakash Samnani, Vadodara

Dr. Sridhar T. M , Chennai

Dr. S. K. Yadav, Vadodara

Dr. A. N. Garg, New Delhi

Advisory Board

Chairman

Dr. Raghaw Saran, Nagpur

Members

Dr. V. Sivanandan Achari, Kochi

Dr. V. Balaram, Hyderabad

Dr. J. Manjanna, Belgavi

Dr. V. R.Nair, Kollam

Dr. Amrit Prakash, Mumbai

Dr. S. Sriman Narayanan, Vellur

Dr. Shivaramu Prasanna, Bengaluru

Dr. K.P. Vijayalakshmi, Trivandrum

Dr. Mohammed Yusuff K.K., Kochi

Dr. Rajeev Raghavan, Trivandrum

Cover page images- curtsey Pixabay.com

Instruction to Authors

- The Manuscript should be typed in **MS word** (times new roman) with **1.5 spacings** and **font size 12**
- The **title** of the paper should be clear and concise(**font size 14 and bold**), the first letter of each noun and adjective in the title must be in capital letter. It will be followed by names of authors(initials followed by surname) with their affiliation (**font size 12**)
- Corresponding author should be indicated by * with email ID
- The text should be divided into following sections:
 - **Abstract : up to 300 words**
 - **Key words: 5-6**
 - **Introduction**
 - **Experimental**
 - **Results and Discussion**
 - **Conclusions**
 - **Acknowledgement**
- Figures and Tables should be before references with a caption **Figures:** Followed by **Tables:**
- **References**
 - Divisions within the section should be indicated as subheadings
 - The figures and tables should be numbered with Roman numerals and must be mentioned in the text at appropriate places
 - Standard abbreviations for technical terms and journals should be used
 - All constants should be expressed in **SI units**
 - References should be numbered consecutively and should appear in the text as superscript at appropriate places.
 - References should be in following pattern
 - For research paper:**
Authors' initials and surname, Journal abbreviation, Volume, Page, Year.
 - For book:**
Authors' initials and surname, Book name, Publisher, Place, Year.
 - For proceedings:**
Authors' initials and surname Proceedings' of the conference name, place, Page, Month and Year.
- The paper is to be submitted in word file and PDF file to isasjournal@isasbharat.in
- After getting the acceptance of the paper, authors have to submit **signed copyright form and undertaking** before publishing the article



Indian Society of Analytical Scientists.



Editorial

It is with immense pleasure that I welcome you to the sixth issue of the Journal of Indian Society of Analytical Scientists (J.ISAS). This issue marks yet another significant milestone in our ongoing journey to explore, understand, and advance the field of analytical science, with a focus on computational chemistry, diffusion in solution, and nano-synthesis.

As we continue to navigate through the ever-expanding landscape of scientific knowledge, the contributions in this issue offer fresh insights, novel approaches, and ground-breaking research findings. In our pursuit of excellence, we have striven to bring forth a collection of research papers that exemplify the dynamism and vibrancy of the analytical sciences in India.


Computational chemistry has witnessed remarkable growth in recent years, and this issue features research paper that delve deep into the intricate world of molecular simulations investigating the reaction mechanism. Understanding the dynamics of molecules in solution is essential for a wide range of applications in various field. The research paper featured here delve into the complexities of diffusion in a solution state, shedding light on how diffusing ions move and interact with their surroundings. Through experimental studies and theoretical modelling, author provides insights into the factors that influence diffusion in gel medium. In a world where sustainable materials and medical advancements are of paramount importance, the research paper on polymer composites hold significant promise and open up a new perspective for applications in biomedicine. Nano-synthesis has become a cornerstone in the development of advanced materials with unique properties and applications The research papers in this issue focus on the synthesis and characterization of nanoparticles, offering a glimpse into the exciting world of nanotechnology. From the controlled growth of metallic

nanoparticles to the design of novel nanocomposites, these contributions showcase how nanosynthesis is at the forefront of innovation. The review of recently published booklet on nanosynthesis, at the end, provides a concise and comprehensive insight and navigates the readers to intricate world of nanotechnology

I want to express my deep appreciation to the authors, reviewers, and the editorial team for their dedication and hard work in bringing this issue to fruition. I wish to express my sincere gratitude towards ISAS president and Advisor of J.ISAS - Dr. Raghav Saran along with the committed individuals on the editorial board, Dr. Vijayalaxmi Adya and Dr. Vinay Bhandari, for their continuous cooperation. I appreciate the technical support extended by Shivani Kantak and Vaibhav Parse.

The success of J.ISAS is a testament to the commitment and passion of the scientific community. I hope that you will find the research papers in this issue as insightful and inspiring. Together, let us continue to foster a culture of analytical excellence and innovation in India, and the world.

Looking forward for your response and articles in future issue.



Dr. Nilima Rajurkar
Editor in Chief
Journal of ISAS

Journal of ISAS

ISSN : 2583-5459

2(2), Pages 1 to 86, (2023)

(An open access Peer reviewed quarterly e- journal by Indian Society of Analytical Scientists)

Contents

S.No.	Title and Authors	Page no.
1	Research Paper: Quantum Chemical Reactivity Investigation on ism Methyl Acetate Through DFT Studies P. Gayathri and P. Udhayakala* *E mail: dean-che@drmgrdu.ac.in DOI: 10.59143/isas.jisas.2.2.METN2363	1-20
2	Research Paper: Preparation of Inorganic Composites of Chitosan/magnesium Oxide Nanoparticle for Antibacterial Activity K. Deepa ¹ , M. Leo Edward ² , A. Shalini ³ and V. Jaisankar ^{4*} * E-mail: vjaisankar@gmail.com DOI: 10.59143/isas.jisas.2.2.KCNA4459	21-30
3	Research Paper: Synthesis Of Graphene Oxide Modified Polyaniline And Its Electrochemical Application For Detection of Nitric Oxide A. Shalini, K.Pandian, K. Deepa and V. Jaisankar * *Email: vjaisankar@gmail.com DOI: 10.59143/isas.jisas.2.2.QONR9019	31-38
4	Research Paper: Diffusion of Fe ³⁺ Ions in Agar Gel Medium Containing Zinc Sulfate: Obstruction effect and Activation Energy M. S. Gupte* *Email: mohinigupte@moderncollegegk.org DOI: 10.59143/isas.jisas.2.2.IAWX1959	39-50
5	Research Paper: Synthesis of Au nanospheres, Au/PVDF nanocomposites and their breath sensing properties Amruta D. Bang, Parag V. Adhyapak *E-mail: adhyapak@cmet.gov.in , adhyapakp@gmail.com DOI: 10.59143/isas.jisas.2.2.QDAI6853	51-62
6	Research Paper: Effect of addition of fillers on Cellulose/ β -TCP polymer Composites: Thermal, Mechanical and Antimicrobial Properties T. S. Kiruthika, B. Deepan Kumar and V. Jaisankar* *Email: vjaisankar@gmail.com DOI: 10.59143/isas.jisas.2.2.NOQE5610	63-84
7	Booklet Review: "Solvothermal and Hydrothermal Techniques for Nano-synthesis: An Overview by Dr. Manisha Bora Dr. Dinesh Amalnerkar *Email: dpa54@yahoo.co.in DOI: 10.59143/isas.jisas.2.2.IZRV7844	85-86

Quantum chemical reactivity investigation on ism methyl acetate through dft studies

P. Gayathri¹ and P. Udhayakala*²

¹ Department of Chemistry, Dr.MGR Educational and Research Institute, Chennai, India

^{2*} Dean, Department of Chemistry, Dr.MGR Educational and Research Institute, Chennai, India

*E mail: dean-che@drmgrdu.ac.in

Received: 12.7.23 Revised: 23.8.23 Accepted: 5.9.23

Abstract

The reliability of the product that will arise from the millions of reactions that are taking place in interstellar medium is dependent on the analysis of the rate constant. The current investigation is a chemical modelling research performed with Density Functional Theory (DFT) studies utilizing a foundation set of B3LYP 6-311++ G (d, p). The hydrolysis of methyl acetate in the interstellar medium is described using the quantum chemical parameters E_{HOMO} (highest occupied molecular orbital energy), E_{LUMO} (lowest unoccupied molecular orbital energy), energy gap (ΔE), chemical potential (μ), hardness (η), softness (S), the absolute electronegativity (χ), nucleophilicity index (N) and the electrophilicity index (ω). In order to study the probable reactive sites of the interstellar chemical methyl acetate in the ISM condition, the local reactivity descriptors Fukui function, NBO, and MEP were analysed in depth. The thermo chemical investigation contributed to the improvement of the chemical reaction mechanism and the calculation of the rate constant of the species under investigation results in the analysis of feasibility of the reaction under study.

Keywords: Interstellar chemistry, Quantum chemical parameters, NBO, MEP, ISM condition, Thermo chemical analysis, Feasibility, Fukui function.

1 Introduction

There is a tremendous variety of molecules in the interstellar medium. It is largely made up of so-called interstellar clouds of gas and dust, which can range in density from dense clouds that can appear dark against the sky to somewhat wispy diffuse clouds that are impenetrable to background light. It is necessary to conduct research into the complex interstellar chemistry, which consists of an abundance of space molecules and generates brand-new molecules every fraction of a second, in order to comprehend the process of new star formation and the development of this process. More than 250 molecules like H_2O , CH^+ , CN , H_2S etc have been identified in interstellar and circumstellar clouds¹, with most interstellar sources having molecules in the gas phase. Both gas-phase activities and reactions on the surfaces of dust grains take place in interstellar clouds, with the latter taking place primarily on and in the water-dominated ice mantles of cold clouds. Some of these processes are extremely unusual by terrestrial standards, particularly when they occur at low temperatures².

In the past few decades, calculations based on quantum chemistry have found applications in a variety of chemical fields, such as the analysis of reaction pathways. This is a result of developments in theory, particularly improvements in the accuracy of functionals based on density functional theory (DFT).

Complex organic molecules and stars are born in the dark and dense environs of the interstellar medium (ISM), which includes everything between stellar systems. In these regions, dust grains covered in H_2O -ice provide the surface necessary for the formation of many organic molecules³.

In the year 1982, the ISM NaOH is discovered in the interstellar medium. This detection represents the first proof of a grain reaction generation mechanism for simple metal hydroxides⁴. Galactic centre source SgrB2 outside has been found to contain methyl acetate⁵. The Atacama Large Millimeter /submillimeter Array (ALMA) has discovered the chemical compound methyl alcohol (methanol) in the TW Hydrae protoplanetary disc. It has never been discovered in a nascent planet-forming disc. The only complex organic compound that clearly originates from an ice state that has been found in discs so far is methanol. Its discovery aids astronomers in their understanding of the chemical processes involved in the formation of planetary

systems, which ultimately result in the production of the building blocks for life ⁶. Using the Berkeley-Illinois-Maryland Association (BIMA) Array and the Caltech Owens Valley Radio Observatory (OVRO) Millimeter Array, the acetic acid (CH_3COOH) in the Sgr B2 Large Molecule Heimat source was discovered ⁷. The IRAM 30 m radio telescope in Orion has recently detected methyl acetate $\text{CH}_3\text{COOCH}_3$, albeit its deuterated isotopomers have not yet been verified to be present. Acetyl CH_3CO and methoxy CH_3O radicals may combine with one another to produce methyl acetate. Using a gas-grain chemical network, we can estimate the abundances of $\text{CH}_3\text{COOCH}_3$, its two singly deuterated isotopomers, and its two isomers (ethyl formate and hydroxy acetone), as well as their two isomers ^{8,9}.

This work employs Density Functional Theory and quantum chemical reactivity descriptors to investigate the hydrolysis of methyl acetate (ISM). We identified a knowledge gap in the DFT-based quantum chemical descriptor. Hydrolysis of interstellar molecules is the focus of the current research, which use B3LYP coupled with the 6-311++ G basis set to examine the process (d, p).

2 Experimental

The reaction mechanism of ISM methyl acetate was investigated in the ISM temperature and pressure using quantum chemical parameters. The experimental rate constant were studied using the rate law linking the concentrations of the reacting species with the rate of the hydrolysis of methyl acetate.

2.1 Materials

All the quantum chemical calculations have been performed at the B3LYP level of theory using Gaussian 16 series of programs.

2.2 Methods

In recent years, there has been a rise in the quantity of publications that are concerned with theoretical calculations in the areas of spectroscopic assignments, the investigation of electronic states and structures, and the clarification of reaction mechanism.

Geometry optimization is the first derivative of energy with respect to atomic location. When the geometry depends on either Cartesian or internal molecule

coordinates, the goal of geometry optimization is to locate the minimum of the corresponding mathematical function. For ISM methyl acetate, HOMO-LUMO values, Mulliken atomic charges, and thermochemistry ideas are provided by a successful geometry optimization utilising Functional Density Function Theory (DFT) with B3LYP connected with basis set 6-311++ G (d, p) at 0 **atmospheric** pressure and 15K temperature ¹⁰. Quantum chemical calculations of ISM ethanol may be found using the Gaussian 16 software.

2.2.1 Frontier Molecular Orbital Studies

The frontier molecular orbital theory (FMO) of chemical reactivity states that, highest occupied molecular orbital (HOMO) and lowest unoccupied molecular orbital (LUMO) of the interacting species interact to cause the transition of the electron ¹¹. The capacity of a molecule to donate and accept electrons is used to define the HOMO and LUMO ¹². The study of molecular electronic characteristics relies heavily on the values of molecular orbitals. Chemical properties like an electrophilicity, hardness, and nucleophilicity are calculated using HOMO and LUMO energies.

Ionization potential (I), electron affinity (A), electronegativity (χ), global hardness (η), and softness (S), Electrophilicity index(ω), Nucleophilicity index(N), can all be expressed in terms of HOMO and LUMO energy, according to **Koopman's** theorem ¹³.

The energy needed to remove an electron from a molecule is known as the ionisation potential (I). Equationally, it is connected to the of HOMO.

$$\text{Ionization energy, } I = -E_{\text{Highest Occupied Molecular Orbital}} \quad (1)$$

The energy released when a proton is introduced to a system is known as electron affinity (A). E_{LUMO} is connected to it via the following equation.

$$\text{Electron Affinity, } A = -E_{\text{Lowest Unoccupied Molecular Orbital}} \quad (2)$$

The ability of an atom or collection of atoms to draw electrons to itself is measured by the electronegativity, which may be calculated using the formula.

$$\text{Electro negativity, } \chi = \frac{\text{Ionisation energy} + \text{Electron affinity}}{2} \quad (3)$$

Chemical hardness (η) is a measure of an atom's resistance to a charge transfer. It is calculated using the following equation.

$$\text{Chemical hardness, } \eta = \frac{\text{Ionisation potential} - \text{Electron Affinity}}{2} \quad (4)$$

Chemical potential is a measure of the capability of a substance to cause either a chemical (or) electrochemical reaction in its environment, due to its internal energy (or) external energy.

$$\text{Chemical potential, } \mu = - (\text{Electro negativity}) \quad (5)$$

Chemical softness (S) is a measure of an atoms or group of atoms ability to accept electrons and is calculated using the equation

$$\text{Softness, } S = \frac{1}{\eta} \quad (6)$$

A reactivity descriptor called electrophilicity index a quantitative classification of a molecule's overall electrophilic nature on a relative scale. The electrophilicity index was described as follows.

$$\text{Electrophilicity index, } \omega = \mu^2 / 2\eta \quad (7)$$

The nucleophilicity N index is a measure of the nucleophilicity of complex organic molecules displaying nucleophilic behaviors.

$$\text{Nucleophilicity index, } N = 1/\omega \quad (8)$$

2.2.2 Fukui Function

With the use of the Fukui function, one can investigate the molecule's reactivity in relation to that of other molecules. It is a representation of the change in external potential in relation to the change in chemical potential when the number of electrons remains the same¹⁴. The greatest values of Fukui functions point to the areas of the molecular surface that are the most reactive. Atoms in a molecule that have the highest possible value of f_k^- indicate the electrophilic attacking centre, whereas atoms with the highest possible value of f_k^+ represent the nucleophilic attacking centre. Therefore, the Fukui function can be utilised to accurately predict the majority of the nucleophilic and electrophilic sites present in the molecule. The finite difference approximation can be used to calculate the nucleophilic f_k^+ and electrophilic f_k^- Fukui functions, which represent the change in electron density¹⁵.

$$f_k^+ = q_{N+1} - q_N \quad (9)$$

$$f_k^- = q_N - q_{N-1} \quad (10)$$

2.2.3 Molecular Electrostatic Potential Analysis

The Molecular Electrostatic Potential of the surface provides an illustration of the three-dimensional charge distribution of the molecule. The MEP surface can glow as a map of areas with an excess of electrons and areas with an electron deficit. The MEP is utilised to recognise patterns of positive and negative potentials that are distinctive of a certain system. The potential energy interaction between proton and electron fields is categorised from high frequency (blue) region to higher wavelength (red) region, which identifies the charge dislocation between electrophilic and nucleophilic boundaries. The blue region has a higher frequency than the red region.

2.2.4 Non-Bonding Orbital Analysis

Natural Bond Orbital (NBO) investigation of ISM methyl acetate is carried out at the B3LYP/6-311++G (d, p) level for the purpose of obtaining information on hybridization as well as the electronic structure of the molecule¹⁶.

2.2.5 Investigation of Reaction Mechanism -Thermochemical Analysis

The favourable energy conditions along with spontaneity studies provided the flow of energy to analyse the pathway in which the Interstellar reaction takes place.

2.2.5.1 Energetics of Reaction

For a reaction to be considered endothermic, the products must offer a net benefit to energy terms that are greater than those offered by the reactants. On the other hand, for an exothermic reaction, the reactants need to be more energetically favourable than the products. This is a prerequisite for an exothermic reaction.

$$E_{\text{reaction}} = E_{\text{product}} - E_{\text{reactant}} \quad (11)$$

2.2.5.2 Spontaneity of the reaction

According to **thermodynamics**, **free** energy means available energy which is used to do useful **work**. **This** free energy is released during spontaneous **reaction**. **A**

spontaneous reaction is one which favoured the product formation in condition in which it take place. Using the reaction's enthalpy and entropy values, Gibb's equation may determine whether the reaction is spontaneous or non-spontaneous. Negative free energy reactions are those that may proceed without spending any more energy.

$$\Delta_r H^0 = \Sigma [(\epsilon_0 + H_{\text{corr}})_{\text{products}}] - \Sigma [(\epsilon_0 + H_{\text{corr}})_{\text{reactants}}] \quad (12)$$

$$\Delta_r G^0 = \Sigma [(\epsilon_0 + G_{\text{corr}})_{\text{products}}] - \Sigma [(\epsilon_0 + G_{\text{corr}})_{\text{reactants}}] \quad (13)$$

2.6 Rates of Reaction

The key equation for calculating reaction rate is

$$k_{(15K)} = \frac{K_B T e^{-\Delta G^0/RT}}{h C^0} \quad (14)$$

3 Results & Discussions

3.1 Structure optimization

Utilizing B3LYP/6-311++G, an optimization of the interstellar molecular structure of ISM methyl acetate Fig. 1 was carried out at a temperature of 15K and a pressure of 0 atmosphere (d, p).

ISM methyl acetate's HOMO Fig.2 and LUMO Fig.3 structures, computed using the B3LYP/6-311++G method d, p).

3.2 Reactivity Parameters Derived from Frontier Molecular Orbitals

The electrophilicity index is used to categorise electrophiles into three different strength levels: **weak** ($\omega < 1.50 \text{ eV}$), **moderate** ($1.50 > \omega > 0.86 \text{ eV}$), and **strong** ($\omega > 1.50 \text{ eV}$). The nucleophiles can be broken down into three different categories: moderate ($N > 3.00 \text{ eV}$), marginal ($N < 2.00 \text{ eV}$), and strong ($N > 3.00 \text{ eV}$)¹⁷. According to this categorization, the ISM methyl acetate act both as an electrophile as well as a nucleophile of significant strength.

Its strong nucleophilic nature in the ISM medium suggests that its chemical reactivity can donate electron density. It exists in the interstellar medium (ISM). Interstellar methyl acetate's chemical behaviour can be analysed by considering the energy gap between its HOMO and LUMO states. Both the chemical and kinetic stability of the molecule can be described here. It also reveals details about the molecular excitation type. For ISM methyl acetate, the energy gap between the HOMO and LUMO states is -0.27615 kJ/mol. Given these factors, it is reasonable to assume that ISM methyl acetate is highly reactive and less stable¹⁸. Therefore, the photochemical activation of isopropyl methyl acetate (ISM) is a simple process.

In this regard, the global electronegativity (χ), the chemical potential (μ), the global hardness (η), the global softness (S), and the electrophilicity index (ω) all have a high degree of success in forecasting the feasibility and character of reaction in the ISM medium. The global softness index and the global electrophilicity index are both calculated by making use of the energy of the border molecular orbitals EHOMO and ELUMO. This is done with the assistance of Koopmans' theorem.

3.3 Fukui functions Derived from Mulliken charges

The findings of the study on the local selectivity¹⁹ indicate that ISM methyl acetate have the capacity to carry out the functions of both an electrophile and a nucleophile. It is anticipated that carbon 8 will be the site of most electrophilic attacks on ISM methyl acetate molecules. The carbon atom at position C3 of methyl acetate in the ISM possesses a nucleophilic attacking centre. It **was observed** from this that methyl acetate in the ISM can go through both electrophilic and nucleophilic processes. To explore the local reactivity, chemical reactivity and site selectivity associated with the ISM methyl acetate, the Fukui function and local electrophilicity/nucleophilicity have been used. By these calculations, it was observed that ISM methyl acetate **undergoes** hydrolysis in presence of water in the Interstellar medium. The 8C atom of ISM methyl acetate molecules contain higher electrophilicity than other hydrogen and carbon atoms. By global and local descriptors, the values of 7O and 3C atoms demonstrate that atom 7O would be the most favourable reaction site and atom 3C atom preferably attacks atom **7O** and, as a further step, 8C and 7C get attached, to form methanol in the interstellar medium. The highest values of 3C confirms that

most **favourable** reaction site for nucleophilic attack which leads to the formation of acetic acid in the **interstellar medium**.

3.4 Interpretation of Relative Polarity- MEP

The colour red indicates a positive extreme (lowest electrostatic potential, which reveals an electrophilic attacking centre) in the MEP figure of ISM methyl acetate, while the colour blue indicates a positive extreme (highest electrostatic potential, which shows a nucleophilic attacking centre)²⁰. As a result of this work, the electrophilic centre of the oxygen atom in ISM methyl acetate is confirmed.

3.5 Analysis of Maximum Electron Density with NBO

Second order perturbation analysis confirms that the stabilization energy of **42. 41** kcal/mol corresponds to conjugative interaction from donor LP (2) of O₃ to $\pi^*C_1-O_2$ and stabilization energy of **33. 13 kcal/mol** corresponds to conjugative interaction from donor LP (2) of O₂ to $\sigma^*C_1-O_3$ which confirms that ISM methyl acetate has three possible resonance **structures**.

Step I: The lone pair electron on LP (1) O₂ in ISM methyl acetate is transferred to protonated water molecule which initiates hydrolysis mechanism by forming first **intermediate (Protonation step)**.

Step II: The lone pair electron on oxygen atom in water is attacking carbonyl carbon in methyl acetate which is confirmed by transition from πC_1-O_2 to $\pi^*C_1-O_2$ corresponds to energy **0.68 K. Cal/mol (Nucleophilic addition)**.

Step III: Proton transfer occurs between another molecule of water and second intermediate.

Step IV: ISM Methanol molecule is eliminated which is confirmed by LP (2) O₃ to $\sigma^*C_8-H_{10}$ and $\sigma^*C_8-H_{11}$ transition corresponds to energy 5.24 kcal/mol. **Further** transition from LP (2) O₃ to $\pi^*C_1-O_2$ having energy 42.41 K. Cal/mol also confirms that ISM methanol molecule is eliminated in this step.

Step V: ISM acetic acid is formed in this **step**. **Once** methanol is eliminated in the step IV, it forms carbocation which undergoes internal electron transfer forming double bond between C₁ to O₂.

3.6 Kinetics of catalytic hydrolysis of methyl acetate

The value of the first order rate constant, k for the acid catalytic hydrolysis of methyl acetate obtained through experimentation is determined to be $2.3 \times 10^{-2} \text{ s}^{-1}$ (Table 5). The current theoretical investigation at temperature 15K and $\Delta_r G^0 = 3.48205 \text{ kcal/mol}$ suggests the rate constant, k as $3.1254 \times 10^{11} \text{ e}^{-116.83} \text{ s}^{-1}$ (Table 4) which corresponds to the experimental value except the theoretical study being done in the gas phase and ISM circumstances exhibiting little alteration in results.

3.7 Energetics of Reaction

Molecules are always broken (hydrolysed) through an endothermic process because it always requires energy to break bonds. An endothermic reaction must have an overall increase in the amount of energy present in the end products when compared to the reactants. **It is known that** the activation energy required to hydrolyse ISM methyl acetate into molecules of ISM acetic acid and methanol is 24.4472 kcal/mol based on the findings of the studies that were previously discussed. The endothermic nature of hydrolysis under the ISM condition is demonstrated graphically and supported by experimental values²². The energy values suggest that the final product of every reaction step has lower energy than the Reactant and TS is formed after crossing the potential barrier. All the calculations suggest the high feasibility of acetic acid and methanol formation in the ISM. The calculations for global and local reactivity descriptor are performed at B3LYP/6–311G (d, p) and are expressed in Table 1 and Table 2. These values indicate the formation of methanol and acetic acid through the soft-soft interaction in methyl acetate. The reaction mechanism for hydrolysis of methyl acetate reaction path is displayed in Fig. 6.

3.8 Spontaneity of a reaction

The change in entropy may be calculated by considering both the change in Gibb's free energy and the change in enthalpy values²³. It has been shown that ΔG is positive for the hydrolysis of ISM methyl acetate. Because of this, it has been shown that the hydrolysis that occurs in the interstellar medium is not a spontaneous response. This hydrolysis is only capable of taking place in the presence of ISM acids or bases. There is evidence to support the viability of interstellar reactions with potential barriers greater than 60 kcal/mol²⁴

4 Conclusion

Using chemical simulation technologies based on DFT methods, the hydrolysis of Interstellar molecule methyl acetate was explored in the ISM condition. Calculations were done to determine the energy levels of the HOMO and LUMO orbitals of the optimised ISM methyl acetate. It was observed that the HOMO-LUMO gap in ISM methyl acetate has a low energy level, which made it easy for electrons to transfer, as confirmed by the NBO analysis of the molecule. The Δ_rH^0 and Δ_rG^0 of hydrolysis reactions of ISM methyl acetate was also calculated. Using these values, it was confirmed that hydrolysis of ISM methyl acetate is non-spontaneous reaction in the interstellar medium. Energetics of reaction investigations confirmed that hydrolysis of ISM methyl acetate is endothermic in the interstellar medium. Kinetics of catalytic hydrolysis of methyl acetate is proven to be first order experimentally. Theoretical calculation of hydrolysis of ISM methyl acetate is likewise found to be first order in kinetics. Experimental and theoretical research have both shown that the rate of hydrolysis is solely dependent on the concentration of methyl acetate and is unrelated to the presence of water in the reaction mixture. Because of this, the hydrolysis of ISM methyl acetate can take place in the ISM medium.

Using quantum chemical techniques, it has been investigated whether the interstellar molecule $\text{CH}_3\text{COOCH}_3$ may produce acetic acid and methyl acetate. The B3LYP theory's quantum chemical calculations showed that the likelihood of their formation combines with the earlier statement. The proposed reaction pathways have large potential barriers, but it is still possible for reactants to pass over the barriers by thermal hopping or quantum tunnelling. The research showed that the synthesis of methanol and acetic acid in the ISM is effective both in the gas phase and in the ice grains. When some energy is available from cosmic and UV rays in the hot core of Sgr B2, the observed energetic study of the hydrolysis of ISM methyl acetate can penetrate. Therefore, there is a high likelihood that methyl acetate will be hydrolysed in ISM.

Figures:

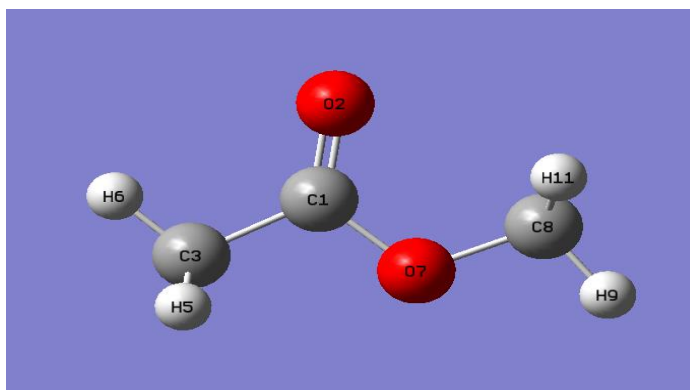


Fig. 1 Optimized structure of ISM Methyl acetate

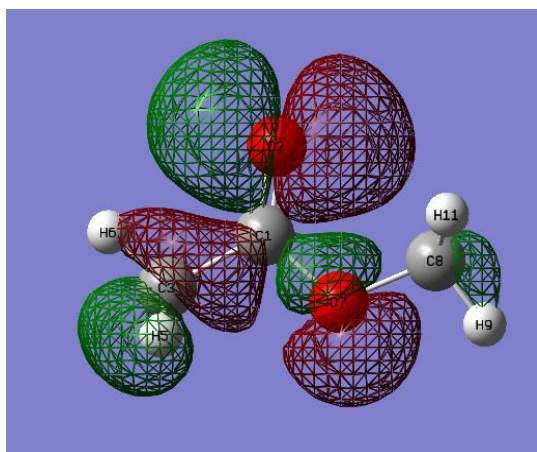


Fig.2 HOMO

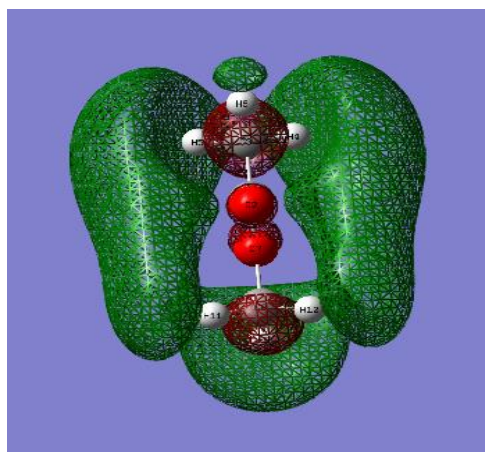


Fig. 3 LUMO

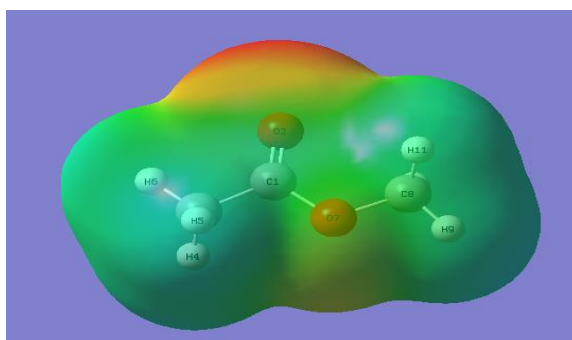


Fig. 4 MEP of ISM Methyl acetate

RESONANCE STRUCTURE

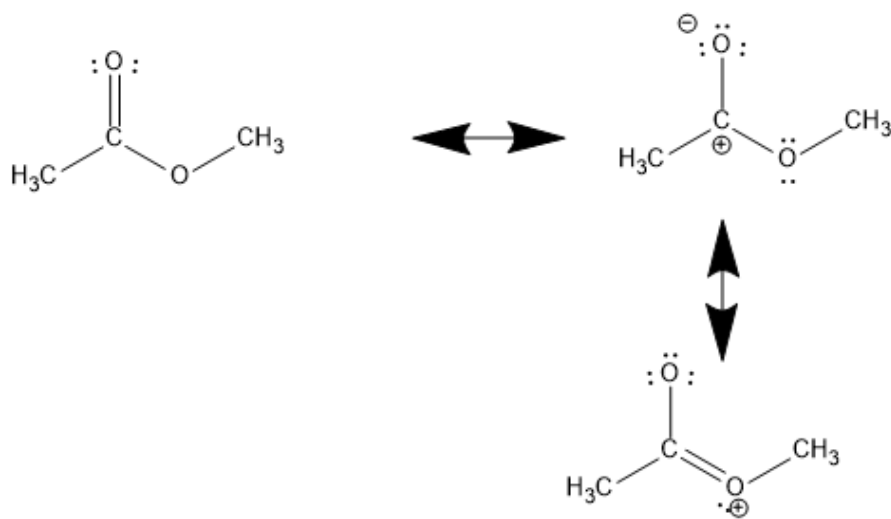
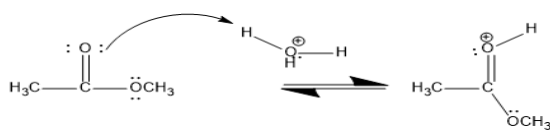
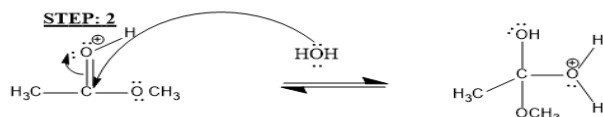


Fig. 5 Resonance structure of methyl acetate

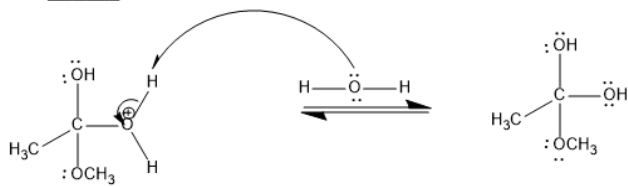
STEP: 1



STEP: 2



STEP: 3



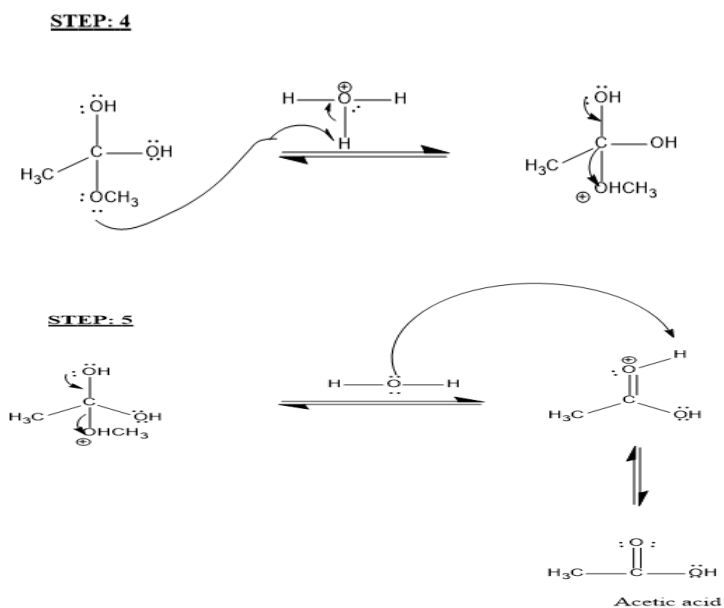


Fig.6 Mechanism of Hydrolysis

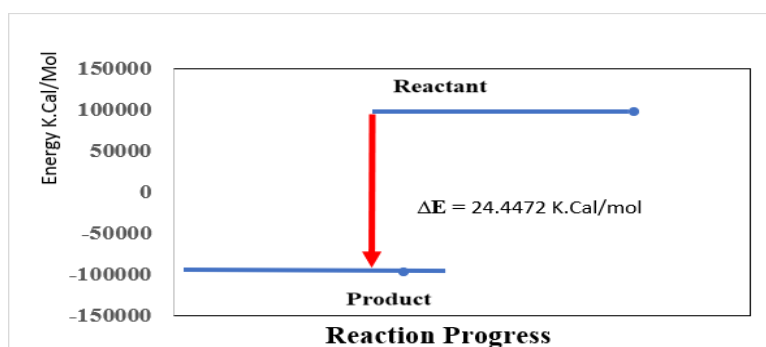


Fig. 7 Reaction Progress for hydrolysis of methyl acetate

Tables:

Table 1. Reactivity Parameters Derived from Frontier Molecular Orbitals

Molecular Properties	B3LYP/6-311d(d,p)
HOMO	-0.28625
LUMO	-0.01010
Energy Gap	-0.27615
I	0.28625
A	0.01010
χ	0.148175
μ	-0.148175
η	0.138075
S	7.2424
ω	0.07952
N	12.5755

Table 2. Fukui functions Derived from Mulliken charges

	qn	qn-1	qn+1	f^{k+} nucleophilic attack	f^{k-} Electrophilic attack)
C	0.167931	0.267923	-0.594776	-0.762707	-0.099992
O	-0.295953	0.133449	-0.347765	-0.051812	-0.429402
C	-0.527905	-0.528272	2.160853	2.688758	0.000367
H	0.174718	0.254283	-0.692777	-0.867495	-0.079565
H	0.174774	0.227328	-0.798313	-0.973087	-0.052554
H	0.168069	0.254261	-0.798238	-0.966307	-0.086192
O	-0.109705	-0.009021	-0.284471	-0.174766	-0.100684
C	-0.247867	-0.270777	1.618567	1.866434	0.022910
H	0.150258	0.219972	-0.562577	-0.712835	-0.069714
H	0.172842	0.230956	-0.562545	-0.735387	-0.058114
H	0.172837	0.219899	-0.137957	-0.310794	-0.047062

Table 3. Second Order Perturbation Analysis of Fock Matrix in NBO Basis of ISM Methyl acetate ²¹

Donor NBO(i)	Acceptor NBO(j)	E ₂ kcal/mol	E(j)-E(i) a.u	F(i,j) a.u
1. σ C ₁ -O ₂	145. σ^* C ₁ -C ₄	1.12	1.45	0.036
	146. σ^* O ₃ -C ₈	1.78	1.35	0.044
2. π C ₁ -O ₂	143. π^* C ₁ -O ₂	0.68	0.40	0.015
	147. σ^* C ₄ -H ₅	1.54	0.77	0.031
	148. σ^* C ₄ -H ₆	1.54	0.77	0.031
4. σ C ₁ -C ₄	142. σ^* C ₁ -O ₂	1.09	1.30	0.034
5. σ O ₃ -C ₈	142. σ^* C ₁ -O ₂	2.70	1.48	0.056
6. σ C ₄ -H ₅	142. σ^* C ₁ -O ₂	1.91	1.17	0.042
	143. π^* C ₁ -O ₂	4.28	0.55	0.045
7. σ C ₄ -H ₆	142. σ^* C ₁ -O ₂	1.91	1.17	0.042
	143. π^* C ₁ -O ₂	4.29	0.55	0.045
8. σ C ₄ -H ₇	142. σ^* C ₁ -O ₂	0.56	1.16	0.023
	144. π^* C ₁ -O ₃	4.91	0.88	0.060
9. σ C ₈ -H ₉	144. σ^* C ₁ -O ₃	3.19	0.89	0.049
10. σ C ₈ -H ₁₀	146. σ^* O ₃ -C ₈	0.56	0.81	0.019
11. σ C ₈ -H ₁₁	146. σ^* O ₃ -C ₈	0.56	0.81	0.019
17. n1 O ₂	144. σ^* C ₁ -O ₃	0.85	1.04	0.027
	145. σ^* C ₁ -C ₄	2.57	1.05	0.047
18. n2 O ₂	144. σ^* C ₁ -O ₃	33.13	0.61	0.129
	145. σ^* C ₁ -C ₄	18.25	0.62	0.097

19.n1O ₃	142.σ*C ₁ -O ₂	2.01	1.19	0.044
	145.σ*C ₁ -C ₄	5.88	0.91	0.066
	150.σ*C ₈ -H ₉	2.80	0.94	0.046
	151.σ*C ₈ -H ₁₀	0.77	0.92	0.024
	152.σ*C ₈ -H ₁₁	0.77	0.92	0.024
20.n2 O ₃	143.π*C ₁ -O ₂	42.41	0.34	0.108
	151.σ*C ₈ -H ₁₀	5.24	0.69	0.056
	152.σ*C ₈ -H ₁₁	5.24	0.69	0.056
143.π*C ₁ -O ₂	147.π*C ₄ -H ₅	0.89	0.37	0.050
	148.π*C ₄ -H ₆	0.89	0.37	0.050
144.σ*C ₁ -O ₃	147.σ*C ₄ -H ₅	1.29	0.03	0.023
	148.σ*C ₄ -H ₆	1.28	0.03	0.023
	149.σ*C ₄ -H ₇	2.47	0.06	0.044
	150.σ*C ₈ -H ₉	1.75	0.03	0.029
	151.σ*C ₈ -H ₁₀	1.16	0.01	0.015
	152.σ*C ₈ -H ₁₁	1.16	0.01	0.015

Table 4. Kinetic data calculated theoretically

Species	Name	Free energy
CH ₃ COOCH ₃	Methyl acetate	-268.386377
H ₂ O	Water	-76.437562
CH ₃ COOH	Acetic acid	-229.104027
CH ₃ OH	Methanol	-115.714538

Table 5. Experimental Results for Rate constants

S.No	Time/min	Titre value V _t	(V _∞ -V _t)	Log((V _∞ -V _t))	Rate constant K=2.303/t X log(V _∞ -V ₀)/ (V _∞ -V _t)
1	0	24.5			
2	10	26.4	14	1.1461	0.0127
3	20	29.2	11.2	1.0492	0.0175
4	30	32.1	8.3	0.9191	0.0217
5	40	34.8	5.6	0.7482	0.0261
6	50	37.9	2.5	0.3979	0.0370
7	∞	40.4			
Rate constant				K=0.023=2.3X10 ⁻² s ⁻¹	

Table 6. Hydrolysis of ISM methyl acetate

Energy	Reactant		Total	Product		Total
	CH ₃ COOCH ₃	H ₂ O		CH ₃ COOH	CH ₃ OH	
E (a.u)	-268.478175	-76.458532	-344.936707	-229.132718	-115.764998	-344.897716
E(K. Cal/mol)	-168472.6054	-47978.43510	-216451.0405	-143782.9573	-72643.63601	-216426.59331
a.u			kcal/mol			
E _{reaction} =E _{product} - E _{reactant}			E _{reaction} =E _{product} - E _{reactant}			
= 0.038807 a. u			= 24.4472 kcal/mol			

Table 7. Enthalpies and Free energies of reaction (Hydrolysis of methyl acetate)

	Reactant		Product	
	CH ₃ COOCH ₃	H ₂ O	CH ₃ COOH	CH ₃ OH
ϵ_0	-268.478175	-76.458532	-229.132718	-115.764998
E_{zpe}	0.089216	0.02129	0.061526	0.051025
E_{tot}	0.089362	0.021432	0.061669	0.051167
H_{corr}	0.089410	0.02148	0.061716	0.051215
G_{corr}	0.088440	0.02097	0.060801	0.050460
$\epsilon_0 + E_{zpe}$	-268.385601	-76.437242	-229.103302	-115.713973
$\epsilon_0 + E_{tot}$	-268.385455	-76.4371	-229.103159	-115.713831
$\epsilon_0 + H_{corr}$	-268385408	-76.437052	-229.103112	-115.713783
$\epsilon_0 + G_{corr}$	-268.386377	-76.437562	-229.104027	-115.714538
$\Delta_r H^0$	3.48895 kcal/mol			
$\Delta_r G^0$	3.48205 kcal/mol			

References

1. <https://science.gsfc.nasa.gov/691/cosmicice/interstellar.html>
2. Ashraf Ali, Andre canosa, David Leisawitz, *Front. Astron. Space Sci*, 9, 1, 2022,
3. Alexander Rosu-Finsen, *Nat. Rev. Chem*, 7(5), 299, 2023.
4. Hollis, J.M, Rhodes, P.J, *Astrophys. J.*, (1982), 540, L107,2000
5. Tercero. B, Kleiner.I, Cernicharo J, H. V. L. Nguyen², A. López¹, and G. M. Muñoz Caro¹, *Astrophys. J. Lett.* ,770 : L13, 1,2013.
6. Catherine Walsh, Ryan A. Loomis, Karin I. Öberg, Mihkel Kama, Merel L. R. van 't Hoff, Tom J. Millar, Yuri Aikawa, Eric Herbst, Susanna L. Widicus Weaver, and Hideko Nomura, *Astrophys. J.*, 823: L10, 1,2016
7. David M. Mehringer, Lewis E. Snyder, Yanti Miao and Frank J. Lovas, *Astrophys. J.*, 480: L71–L74, 1997
8. Ankan Das, Liton Majumdar, Dipen Sahu, Prasanta Gorai, B Sivaraman, and Sandip K. Chakrabarti, *Astrophys. J.*, 808, 1,2015
9. Yukiki Y. Yarnall, Reggie L. Hudson, *Spectrochim.Acta A*, 283, 1, 2022

10. Akash Kothari, Linglan Zhu, Jon Babi, Natalie Galant, Anita Ragyanszki, Imre Csizmadia, *J. Life Sci.*, 14, 12, 2020.
11. Ahmed. Y. Musa, Abdul Amir H. Kadhum, A.B. Mohamad, Abdalhamid Ahmad B. Rahoma, *J. Mol. Struct.* 969(1-3), 233, 2010
12. B Gomez, N.V. Likhanova, M A Dominguez-Aguilar, R Martinez-Palou, Alberto vela, Jose L Gazquez, *J. Phys. Chem. B*, 110, 8928, 2006.
13. P Geerlings, F De Proft W Langenaeker, *PubMed Chem Rev.*, 103, 1793, 2003
14. S. Ramalingam, S. Periandy.Sugunakala, T. Prabhu, M. Bououdina, *Spectrochim. Acta A*, 115, 118, 2013
15. MA Quijano, Manuel Palomar, A. Cuan, Mario Romero-Romo, *Int. J. Electrochem. Sci.*, 6(9), 3729, 2011
16. E.D. Glendening, F. Weinhold, AE Reed, JE Carpenter, *J. Comput. Chem*, 34, 1429, 2013
17. P, Z.T.Yilmaz, H.Yasin Odabasoglu, V.Adimcilar, T.Erdogan, A.D.Ozdemir, A.Golcu, M.Odabasoglu, *J. Mol. Struct*, 1205, 1, 2020
18. Marzieh Miar, Abolfazl Shiroudi, Farhad Hatamjafari, Khalil Pourshamsian, Ahmad Reza Oliaey, *J. Chem. Res.*,1, 1, 2020.
19. P. Udhayakala, T.V. Rajendiran, Sethu Gunasekaran, *J. Chem. Pharm. Res.*, 6(4), 1027, 2014
20. Sameh Guidara, Habib Feki, Younes Abid, *J. Mol. Struct.*, 1080, 176, 2015
21. M. Szafran, A. Komasa, E. Bartoszka Adamska, *J. Mol. Struct.*, 827, 101, 2007.
22. Prosper Ikhazuangbe, Kenneth Kennedy Adama, *IJCCP*, 7, 12, 2021.
23. I.M. Kolesnikov,” Thermodynamics of spontaneous reaction and non-spontaneous process”, Nova science publishers, New York, 2001
24. .Woon, D. E. 2002, *Int. J. Quantum Chem*, 855, 305, 2006

Preparation of inorganic composites of chitosan/magnesium oxide nanoparticle for antibacterial activity

K. Deepa¹, M. Leo Edward², A. Shalini³ and V. Jaisankar^{4*}

^{1*}Department of Chemistry, Chellammal Women's College, Chennai –600032, Tamil Nadu, India.

²Department of Chemistry, C. Kandaswami Naidu College for Men, Chennai –600102, Tamil Nadu, India.

³Department of Chemistry, Bhaktavatsalam Memorial College for Women, Chennai –600080, Tamil Nadu, India.

^{4*}PG and Research Department of Chemistry, Presidency College, Chennai –600005, Tamil Nadu, India.

* E-mail: vjaisankar@gmail.com

Received: 16.7.23 Revised: 20.7.23, 18.9.23, 12.10.23 Accepted: 15.10.23

Abstract

Natural polymer based nanocomposites have received attention in research due their biocompatible nature and their versatile application in medical field. In the current investigation, we report the synthesise of chitosan /magnesium oxide nanoparticle (CS/MgO) composite material. The prepared sample was characterized by analytical methods such as FTIR, XRD and HRSEM. The antibacterial activity of the CS/MgO composite was evaluated. FT-IR spectral results showed the CS/MgO composite has distinctive functional groups. HR-SEM images revealed that the formation of well dispersed MgO nanoparticles in CS and it is observed that the MgO nanoparticles are embedded between the functional moieties present in the chitosan which shows the good interaction between chitosan and MgO nanoparticles. The antibacterial activity of the composite was evaluated against *Staphylococcus aureus* and *Escherichia coli*. It is observed that the CS/MgO composite material showed comparatively higher inhibition against *E. coli* than *S.aureus*.

Keywords: Chitosan, magnesium oxide nanoparticles; spectral studies; antibacterial activity.

Introduction

In medical field, a novel biocomposite material is being developed to meet the demands of materials for regeneration and tissue engineering. Among these, polymer composites are made up of metal oxide nanoparticle and polymers materials exhibit distinctive structural and biological features comparable and used to hybrid biological systems in development of bones. Polymer nanocomposites are widely used in biomedical coatings which are designed using metal oxide nanoparticle components with their polymeric mate¹.

Chitosan (CS) is a naturally biopolymer and it possesses a potential to be utilised to generate films, fibres, beads, and dust is obtained by deacetylation of chitin found in crab shells^{2,3}. Due to its antimicrobial qualities and biocompatibility, chitosan has gained prominence for use in biomedical applications, wound dressings, lipid-sequestering agents, hydrogels, blood anticoagulants, blood separation membranes, contact lenses, controlled drug release, and food packaging components⁴⁻⁸. Despite the presence of hydrogen interactions between amino and hydroxyl groups in the CS, certain challenges are encountered. Having limited strength, being unable to dissolve in common solvents, and lacking stability in the body are some of the drawbacks⁹⁻¹².

Polymeric materials are employed in biomedical application are often synthetic polymers such as poly(lactide-co-glycolic) acid, polydopamine, polylactic acid, poly(-caprolactone), polyurethane, and synthetic resin such as collagen, chitosan (CS), and cellulose¹³⁻¹⁸. Metal oxide nanoparticle is used in the preparation of polymeric composites are carbon, ceramics, metal, and metal oxides.¹⁹⁻²⁴. However, coatings comprising only polymers continually have significant downsides. For example, polymers are frequently adaptable but need mechanical strength and chemical stability. The other limited factors of the biomedical applications of polymers are usually not homogeneous, molecular weight distribution and functionalizable in nature^{25,26}. Because has poor adhesion to surfaces, do not effectively create a protective layer, have a tendency to aggregate, may harm cells and they are not suitable for use in medical coatings²⁷.

In the present investigation, we discuss the fabrication of a composite film that includes CS and MgO nanoparticle as well as the assessment of its antibacterial effects. The film composite material was prepared by solvent casting method and characterized by Fourier

transform infrared spectroscopy, X-ray diffraction and High resolution scanning electron microscopy. Also, antimicrobial activity of the prepared composite material was evaluated.

Experimental

Materials

Magnesium sulphate heptahydrate ($\text{MgSO}_4 \cdot 7\text{H}_2\text{O}$; 99%), sodium hydroxide, and acetic acid chemicals were provided by Sigma-Aldrich. Chitosan was purchased from Merck. De-ionized water that has undergone two distillations was used for the experiment. Each and every reagent used in the experiment was of analytical quality.

Preparation of magnesium oxide nano particles

The magnesium oxide nanoparticles were synthesized as the stabilizer by green synthesis approach as well as solution-combustion method²⁸. The starting materials used for the synthesis were magnesium sulphate heptahydrate ($\text{MgSO}_4 \cdot 7\text{H}_2\text{O}$) and acetic acid. In a MgO-NPs synthesis, 1:1 molar ratio of magnesium sulphate and acetic acid was dissolved in distilled water along with stirring for few minutes and 20 mL of *Plectranthus ambonicus* (*Karpuravalli*) extract and 5 mL of water were taken in a titration flask and the solution was heated up to 80 °C for efficient extraction. The reaction mixture was then allowed to cool down to 30 °C and 0.1 M solution of $\text{MgSO}_4 \cdot 7\text{H}_2\text{O}$ was dropwise added into the reaction assembly. The reaction was allowed to proceed for 12 hrs. The acquired greenish white precipitates were filtered, washed and dried in an oven for 2 h to get the MgO-NPs. The prepared NPs were stored in an airtight sample bottle.

Extraction of chitosan from (*Penaeus monodon* shell)

The used raw black tiger shrimp shell (*P. monodon* shell) for the extraction of chitosan as reported in our previous paper²⁹.

Preparation of polymer nanocomposites

Synthesis of polymer nanocomposites chitosan - MgO nanoparticle was prepared by solution mixing method as follows: 0.6 g of chitosan was dissolved in 20 mL of CH_3COOH and 0.2 g of MgO nanoparticle was dispersed separately using magnetic stirrer. After an hour of dispersion, the MgO nanoparticle was added to chitosan solution. The stirring was continued for 24 h in order to get well dispersed chitosan - MgO nanocomposites. The obtained product

was poured into clean Petri dish and the nanocomposite was kept in an oven at 60°C to remove moisture and excess solvent for two days. The prepared chitosan - MgO nanocomposites was used for characterisation studies.

Preparation of antibacterial activity assay (Agar disc diffusion method)

For the preparation of inoculums, stock cultures were maintained at 4 °C on nutrient agar slant. A test tube was filled with nutrient broth. To this broth a loop full of culture was added and the contents of the test tube were incubated for about 24 h at 37 °C. Agar diffusion method was chosen to perform this assay. In the present study, Muller Hinton Agar (MHA) medium was taken. To a petri plate Muller Hinton Agar (MHA) medium was drizzled and allowed to get solidified. The inoculums were placed with the bacterial suspension on solid plates with sterile swab moistened. 20 µl of chitosan - MgO nanocomposite (Concentration: 1000 µg, 750 µg and 500 µg) was placed in the disk. The assay experiment had been incubated for 24 h at 37 °C.

Results and discussion

FT-IR spectroscopy of chitosan - MgO composite

The FTIR spectra of chitosan - MgO composite were recorded in the wave number range of between 4000 and 500 cm^{-1} (Fig. 1). In the MgO NPs, the broad peak (-OH) hydroxyl stretching vibration is observed at 3291 cm^{-1} , which corresponds to the absorbed water molecules³⁰. The metal-oxygen peaks found in the wave number range of between 500 and 800 cm^{-1} . It confirms the stretching vibrations between magnesium and oxygen (Mg-O)^{31,32}. Mg-O stretching bands are observed at 682 and 598 cm^{-1} . The chitosan main broad -OH and -NH peaks with hydrogen bond at 3309 cm^{-1} and 1640 cm^{-1} . It revealing the amide group (C-O stretching along with the N-H deformation mode). The peak at 1375 cm^{-1} is due to the COO- group of carboxylic acid salt, 1047 cm^{-1} is attributed to the C-O-C bonds in glucose circle³³. However, with the CS-MgO NPs, hydrogen bond is observed at 3318 cm^{-1} (-OH and -NH), 2934 cm^{-1} (C-H asymmetric), 2856 cm^{-1} (C-H symmetric stretching), 1591 cm^{-1} (N-H deformation groups), 1408 cm^{-1} (amine (C-N) axial deformation) and 1378 cm^{-1} (-COO carboxylic group)³⁴ and 667 and 548 cm^{-1} (Mg-O stretching bands), respectively. From the results, it was decided that chitosan can form strong and high intermolecular hydrogen bond with MgO.

XRD analysis

The XRD design of CS/MgO is portrayed in Fig 3. A wide peak at $2\theta = 19.92^\circ$ within the XRD design of the compound. The polymer CS indicates amorphous in nature. The CS/MgO composite film exhibits an XRD pattern with a highest point occurs around $2\theta = 20^\circ$, and this is caused by the amorphous CS. The XRD pattern of the CS/MgO film shows three peaks at angles 39.97° , 58.91° and 62.15° in addition to the broad peak at $2\theta = 20^\circ$. The arrangement of magnesium oxide particles is a cube-like structure. The planes of the oxide have a matching with the numbers (JCPDS No. 4-829) in the corresponding to (111), (110), and (220) planes. Pure MgO powder's XRD pattern shows crystalline peaks with high intensity 2θ at 37.72° , 42.76° , 58.81° and 62.08° . The MgO peaks migrated towards higher 2θ value of XRD pattern of the CS/MgO film exhibited distinct variations from that of pure MgO powder and the peak at 42.76° was not visible. Furthermore, compared to pure MgO, the CS/MgO film intensity of the MgO crests essentially diminished (Fig 3). According to the chitosan/MgO composite was successfully made by dispersing MgO nanoparticles into the CS matrix.

HR-SEM analysis

Using HR-SEM, surface morphology was determined of the chitosan - MgO composite film is shown in Fig. 4. The chitosan - MgO composite film can be seen in different magnifications through the images are presented. The CS/MgO film appeared to be uneven and wrinkled when observed at a low magnification. There were a multitude of small openings and slit shaped holes scattered across it. Fig.3a. MgO nanoparticles were described as needle-like platelets with an average diameter and thickness of 75 nm and 27 nm in Fig.3b. The HR-SEM image at a greater magnification of 50 k is remarkable for revealing the margins of multiple MgO nanoplates which proved that the MgO nanoplates were implanted within the CS framework.

Antibacterial activity assay

The antibacterial activity of chitosan - MgO nanocomposite was analysed against two microorganisms which are gram-negative bacteria (*E. Coli*) and one gram-positive bacteria (*S. aureus*) (Table 1). The antimicrobial activity was then determined by calculating the

inhibition zone diameter (Fig. 5). The observation indicates that CS/MgO composite have *E. coli* shows high inhibition zone than *S. aureus*³⁵.

Conclusion

In this investigation, we report the synthesis of a safe and highly biocompatible polymeric nanocomposite containing MgO nanoparticles embedded in a chitosan biopolymer. The composite film of CS/MgO various analytical techniques like Fourier transform infrared spectroscopy, X-ray diffractometry and Field-emission scanning electron microscopy were employed to examine the composite. The antibacterial performance of CS/MgO composite was screened against *E. coli* and *S. aureus*. CS/MgO composite showed good antibacterial activity. The antibacterial activity of the composite was comparatively higher against *E. coli* than *S. aureus*. Thus, the CS/MgO composite can serve as a good biomaterial for bone tissue engineering and clinical applications.

Figures



Fig.1 Photograph of CS/MgO composite film

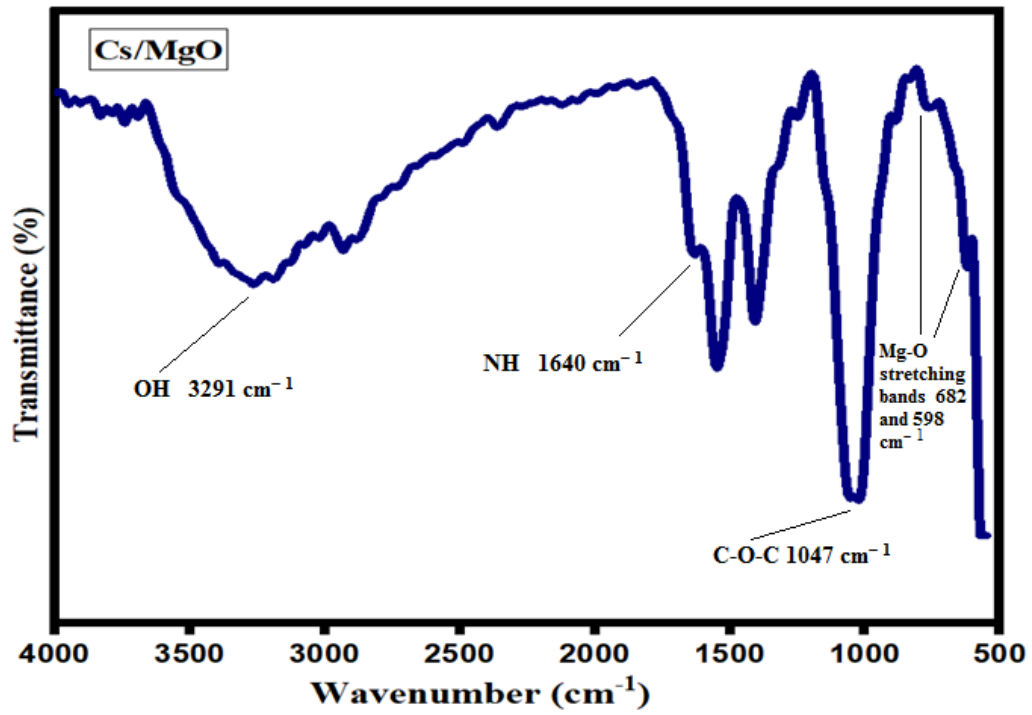


Fig. 2 FTIR spectrum of chitosan – MgO composite

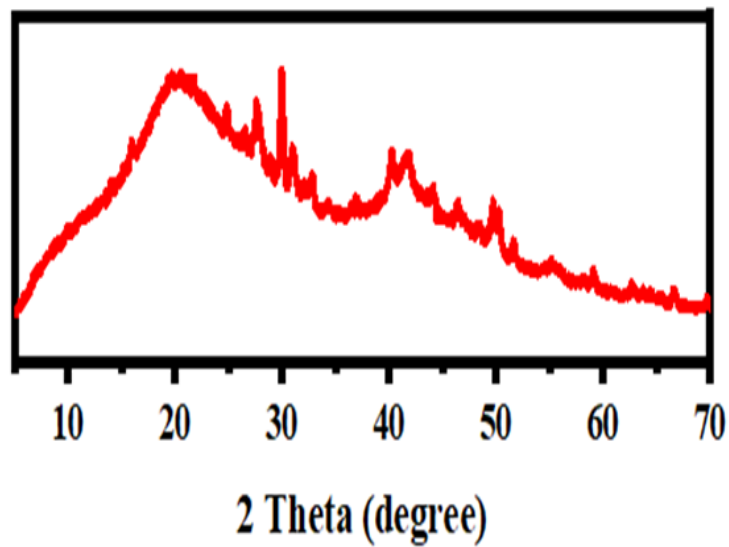
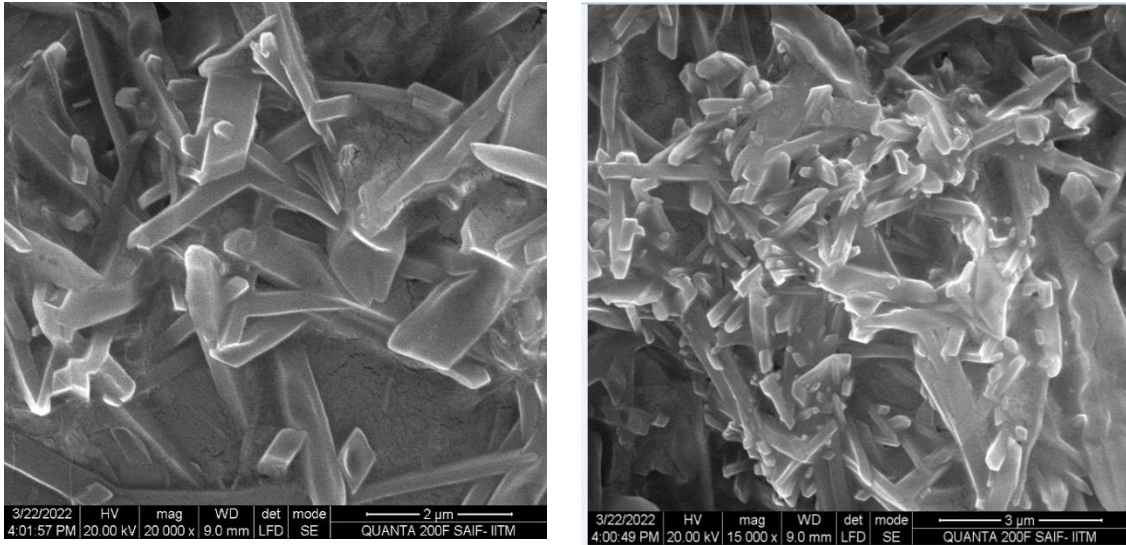


Fig. 3 XRD analysis of chitosan – MgO composite



(a)

(b)

Fig. 4 (a) and (b) HR-SEM images of chitosan – MgO composite at 2 μm and 3 μm resolution respectively



S. aureus



E. coli

Fig.5. Antibacterial efficacy of CS/MGO composite

Table

Table: 1 Antibacterial activity of CS/MgO composite - zone of inhibition (mm)

Organisms	Zone of Inhibition (mm)			
	Sample (µg/ml)			Standard Anti Anti (20µl/disc)
	1000	750	500	
<i>Staphylococcus aureus</i>	10	10	9	14
<i>Escherichia coli</i>	10	10	10	10

References:

1. A. Sharma, G.R. Kokil, Y. He, B. Lowe, A. Salam, T.A. Altalhi, Q. Ye, and T. Kumeria, *Bioactive Materials.*, 24, 535, 2023.
2. K. T. Karthikeyan, A. Nithya and K. Jothivenkatachalam, *International Journal of Biological Macromolecules.*, 104, 1762, 2017.
3. Y. Gutha, J.L. Pathak, W. Zhang, Y. Zhang, X. Jiao, *Int. J. Biol. Macromol.*, 103, 234, 2017.
4. H.N. Lim, N.M. Huang, C.H. Loo, *J. Non-Cryst. Solids.*, 358, 525, 2012.
5. M. Dash, F. Chiellini, R.M. Ottenbrite, E. Chiellini, *Prog. Polym. Sci.*, 36, 981, 2011.
6. M. Rinaudo, *Prog. Polym. Sci.*, 31, 603, 2006.
7. M.N.R. Kumar, *React. Funct. Polym.*, 46, 1, 2000.
8. Honarkar, H.; Barikani, M. *Monatshefte fur Chemie.*, 140, 1403, 2009.
9. E. Szymanska, K. Winnicka, *Mar. Drugs.*, 13, 1819, 2015.
10. A. Anitha, S. Sowmya, P.T.S. Kumar, S. Deepthi, K.P. Chennazhi, H. Ehrlich, M. Tsurkan, R. Jayakumar, *Prog. Polym. Sci.*, 39, 1644, 2014.
11. L. Shao, X. Chang, Y. Zhang, Y. Huang, Y. Yao, Z. Guo, *Appl. Surf. Sci.*, 280, 989, 2013.
12. M. Rodríguez-Vázquez, B. Vega-Ruiz, R. Ramos-Zúñiga, D.A. Saldaña-Koppel, L.F. Quiñones-Olvera, *Biomed Res. Int.*, 821279, 2015.
13. L.Y. Li, L.Y. Cui, R.C. Zeng, S.Q. Li, X.B. Chen, Y.F. Zheng, M.B. Kannan, *Acta Biomater.*, 79, 23, 2018.
14. Y. Liu, K. Ai, L. Lu, *Chem. Rev.*, 114, 5057, 2014.

15. A. Kausar, *Polym. Int.*, 67, 1470, 2018.
16. E. Avcu, F.E. Bas, tan, H.Z. Abdullah, M.A.U. Rehman, Y.Y. Avcu, A.R. Boccaccini, *Prog. Mater. Sci.*, 103, 69, 2019.
17. J. Li, R. Cha, K. Mou, X. Zhao, K. Long, H. Luo, F. Zhou, X. Jiang, *Adv. Healthcare Mater.*, 7, 1800334, 2018.
18. S.Y. Bhong, N. More, M. Choppadandi, G. Kapusetti, *SN Appl. Sci.*, 1, 2019.
19. S. Balasubramanian, B. Gurumurthy, A. Balasubramanian, *Int. J. Pharma Sci. Res.*, 8, 4950, 2017.
20. F. Faupel, V. Zaporojtchenko, T. Strunskus, M. Elbahri, *Adv. Eng. Mater.*, 12, 1177, 2010.
21. S. Sarkar, E. Guibal, F. Quignard, A.K. SenGupta, *J. Nanopart. Res.*, 14, 2012.
22. H.P.S. Abdul Khalil, E.W.N. Chong, F.A.T. Owolabi, M. Asniza, Y. Y Tye, S. Rizal, et al., *J. Appl. Polym. Sci.*, 136, 47251, 2019.
23. D. Moura, J.F. Mano, M.C. Paiva, N.M. Alves, *Sci. Technol. Adv. Mater.*, 17, 626, 2016.
24. M. Alizadeh-Osgouei, Y. Li, C. Wen, *Bioact. Mater.*, 4, 22, 2019.
25. V.M. Esquerdo, T.R.S. Cadaval Jr., G.L. Dotto, L.A.A. Pinto, *J. Colloid Interface Sci.* 424, 7, 2014.
26. D. Liu, Z. Li, Y. Zhu, Z. Li, R. Kumar, *Carbohydr. Polym.*, 111, 469, 2014.
27. N.K. Nga, H.D. Chinh, P.T.T. Hong, T.Q. Huy, *J. Polym. Environ.*, 25, 146, 2017.
28. Kaur, Sukhpreet, J.Singh, R. Rawat, Sanjeev Kumar, Harpreet Kaur, K. Venkateswara Rao, and Mohit Rawat, *Journal of Materials Science: Materials in Electronics.*, 29, 11679, 2018.
29. M. Leo Edward, K. C. Dharanibalaji, K. Thileep Kumar, A. Raghu Subash Chandrabose, A. M. Shanmugaraj, and V. Jaisankar, *Polymer Bulletin.*, 1, 2022.
30. M. Rezaei, M. Khajenoori, B. Nematollahi, *Powder Technol.*, 205, 112, 2011.
31. B.M. Choudary, R.S. Mulukutla, K.J. Klabunde, *J. Am. Chem. Soc.*, 125, 2020, 2003.
32. L. Ai, H. Yue, J. Jiang, *Nanoscale.*, 4, 5401, 2012.
33. F. Tian, Y. Liu, K. Hu, B. Zhao, *J. Mater. Sci.*, 38, 4709, 2003
34. J. Zhou, S. Yang, J. Yu, *Colloids Surf. A Physicochem. Eng. Asp.*, 379, 102, 2011.
35. I.B. Amor, H. Hemmami, S. E. Laouini, H.B. Temam, H. Zaoui, and A. Barhoum, *World Journal of Microbiology and Biotechnology.*, 39, 19, 2023.

Synthesis of Graphene Oxide modified Polyaniline and its electrochemical application for detection of Nitric Oxide

A. Shalini^{1,4}, K.Pandian², K. Deepa³ and V. Jaisankar^{4*}

¹Department of Chemistry, Bhaktavatsalam Memorial College for Women, Chennai –600080, Tamil Nadu, India.

² Department of Inorganic Chemistry, University of Madras, Chennai –600025, Tamil Nadu, India.

³Department of Chemistry, Chellammal Women's College, Chennai –600032, Tamil Nadu, India.

^{4*}PG and Research Department of Chemistry, Presidency College, Chennai –600005, Tamil Nadu, India.

* E-mail: vjaisankar@gmail.com

Received: 16.7.23 Revised: 20.7.23, 21.9.23, 5.10.23 , 14.10.23 Accepted: 15.10.23

Abstract

Nitric oxide plays a crucial and important role in cellular physiology and also functions as a human cancer signaling molecule. Nitric oxide (NO) also exhibits antimicrobial and antitumor properties. However, conventional detection methods have their own limitations in the detection of NO at low concentrations because of its high reactivity and low lifetime. Here, we report a strategy to graphene oxide (GO)-modified polyaniline with efficiency to detect NO at a low concentration by electrocatalytic method. For this study we prepared graphene oxide –polyaniline (GO-PANI) which has higher stability and stronger catalytic activity towards the oxidation of nitric oxide (NO). The synthesized compound was characterized by field emission scanning electron microscopy (FESEM) and UV-visible spectroscopy. With further modification of Nafion, the determination of NO in PBS with different concentration. This investigation offers a different method for determination of NO.

Keywords: Graphene oxide (GO), Polyaniline(PANI), Nitric oxide(NO), Sensing, Cyclic Voltammetry .

1. Introduction

Nitric oxide (NO) has been extensively researched as a result of impact on air pollution, particularly on biological systems. Numerous physiological and pathological processes include it¹. The aberrant generation of NO has an impact on several critical biological activities and contributes to a variety of illnesses². Arteriosclerosis, hypertension, brain

attack, Paralysis agitans and diabetes mellitus (type I and II) can all result from the under or over production of NO^{3,4}. It is crucial from an industrial, biochemical, and medical standpoint either in vivo or in vitro testing to measure the NO produced in healthy and unhealthy tissues⁵. As a result, identification of NO is critical in these fields. The measurement of NO is challenging due to the hydrophobic free radical's automatic chemical reactivity and short half-life (about 6 seconds)²⁻⁶.

Due to its superior attributes, including its quick response, high sensitivity, low cost and most importantly, its suitability for both in vivo and in vitro detection, the electrochemical approach is frequently used⁸⁻¹¹. Other techniques include fluorescence, chemiluminescence, electron spin resonance spectroscopy and UV-visible spectroscopy. Recently, a lot of research has been done on how to modify electrodes with nonmaterials to increase the sensitivity of electrochemical sensor¹². As a result of exceptional biocompatibility, a significant productivity, good conducting ability, intriguing digital transmission capability, and extraordinarily crucial significant particular dimension, graphene is gathered significant interest in electrochemical NO sensors¹³⁻¹⁶. Chemical and electrochemical processes are used to prepare graphene.

A toxic chemical reagent, such as hydrazine, is utilized in a chemical method to reduce graphene oxide (GO) to graphene. The electrochemical approach is high precise and environmentally responsible than this method¹⁷. Graphene-metal nanocomposites have recently been studied for electrochemical sensors^{18-20,29}.

Polyaniline (PANI) is unique among conducting polymers due to its ease of production, excellent conductivity, stability, and low cost²¹⁻²². Many substrates have been detected using PANI-based electrochemical sensors²³⁻²⁵.

Here, an electrochemically reduced graphene oxide (ErGO)-PANI-enhanced Ag electrode was used to create a sensitive and stable NO sensor. The field emission scanning electron microscopy (FESEM) and UV-vis spectroscopy were utilized to explain the rGO-PANI-Ag NPs nanocomposite. To stop interfering species from penetrating the redesigned electrode, a Nafion coating was applied. Using cyclic voltammetry (CV) and chronoamperometry (CA) techniques, the response of the electrochemical and electrocatalytic reaction the resulting Nafion/ PANI-rGO/Ag electrode was studied. It was discovered that the modified electrode had excellent NO oxidation capability.

2. Experimental Methods

2.1. Materials

Graphite fine powder and aniline were purchased from Sigma Aldrichin. In order to create phosphahate buffer saline solutions (BS,0.1M,pH 7.4) 80g of NaCl ,2g KCl ,14.4g Na₂HPO₄ and KH₂PO₄ in one liter distilled water and used as supporting electrolyte ².All solutions are prepared using double distilled water.

2.2. Preparation of NO Standard Solutions

NO was produced by drop wise addition of 2M H₂SO₄ into a saturated NaNO₂ solution .This gas was formed by adding 2M H₂SO₄ drops at a time into a glass flask that already contained saturated NaNO₂ solution .The generated gas was continuously passed through 5%(w/v) pyrogallol solutions in the saturated and 10% (W/V) potassium hydroxide solutions, respectively, to remove oxygen and nitrogen oxides. The full process took place inside the glove box .The glove box and all equipments were meticulously degassed with nitrogen gas for 30min to remove O₂ because the generated NO could react quickly with O₂.At 20°C,the solutions saturated NO concentration was 1.8mM .10mL of deoxygenated PBS (pH 7.0) containing 0.1NaCl was bubbled with produced NO gas for 30min to produce a saturated NO solution .These prepared substance were stored in a glass flask with a rubber stopper ,a light –bocking curtain, and foil-wrapped foils.

2.3. Preparation of PANI-GO

GO was created using Hummer's method from graphite²⁷.Chemical oxidative polymerization was used for producing the PANI-GO nanocomposite²⁸. 17ml of DDW were mixed with 2mg of aniline ,10mg of GO and 0.2mL of 1M HCl for 30min at room temperature.After 4hours of continuous stirring ,10mg of ammonium peroxydisulfate was added to the suspension.Final product was autoclaved at 120° C for 3h.

3. Result and Discussion

3.1. Spectroscopic Study

A UV –vis measurement utilized to describe the manner in which the GO-PANI compositewas produced.The UV-visible spectra of GO,PANI and GO-PANI composite

appear in Fig 1. The $n \rightarrow \pi^*$ transition of C=O groups and $\pi-\pi^*$ transition of aromatic C=C bonds respectively, are related to the two distinctive absorption peaks at 230nm and 300nm that are present in GO. As can be seen, when GO-PANI is used as compared to GO, the maximum absorption peak is discovered to red shift towards 270nm. This change shows that the electronic conjugation in graphene sheets has been refreshed. The transfer of the shared electrons from the polymerization of aniline to the nearby oxygen-containing species on GO is one conceivable reduction mechanism²⁸. Additionally, a peak at 320nm is seen, denoting the formation of PANI.

3.2. Surface Characterization

The morphology of the synthesized materials was evaluated using the FESEM technique Fig .2 Graphene oxide has uniform and neat sheets. On the other hand, the graphene oxide /polyaniline composites Fig .2B is observed as non-uniform sheets in which polyaniline is positioned between the sheets, which indicates the formation of polyaniline particles on flat and uniform graphene oxide sheets²⁸.

3.3. Electrochemical process and amperometric reaction of NO on Nafion /GO/GO-Polyaniline/Ag Electrode

Fig .3 demonstrates cyclic voltammograms of the Nafion/GO/GO-PANI Ag electrode in absence and presence (different concentrations) of NO in oxygen-free 0.1 M PBS (pH 7.0) solution with a scan rate of 100mVs⁻¹. In accordance with Fig PBS does not exhibit a redox peak at pH 7.0, whereas based on the applied voltage range (0 to 1V) the modified electrode showed no response in the absence of NO but an oxidation peak current in +0.8V when NO was present. When compared to the absence of NO, a significant increase in the oxidation peak suggests that NO is being oxidized electrocatalytically. Based on the outcomes, the chronoamperometry(CA) experiments in Fig 4 were performed with a +0.8V applied potential in comparison to the reference electrode²⁶⁻²⁷.

4. Conclusion

In a broader sense we constructed a selective NO sensor based on GO-GO PANI hybrid compound. The interference compounds (NO^{2-} , AA and H_2O_2) were eliminated by nafion. In addition, this compound sensor exhibits high sensitivity and stability, fast response and excellent selectivity for NO identification even with competing species available. The

methodology placed out in this work might serve as a foundation for further investigation to improve the accuracy and speed of NO detection in biological systems, highly conductive polymer-graphene nanocomposites are being used in sensors and biosensors.

Figures

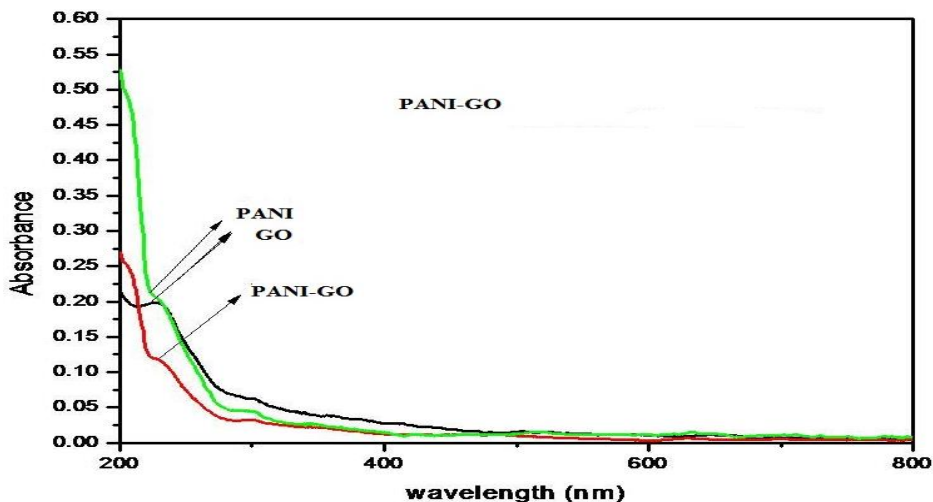


Fig .1 UV-visible Spectra of Graphene oxide /Polyaniline ,Graphene Oxide – Polyailine

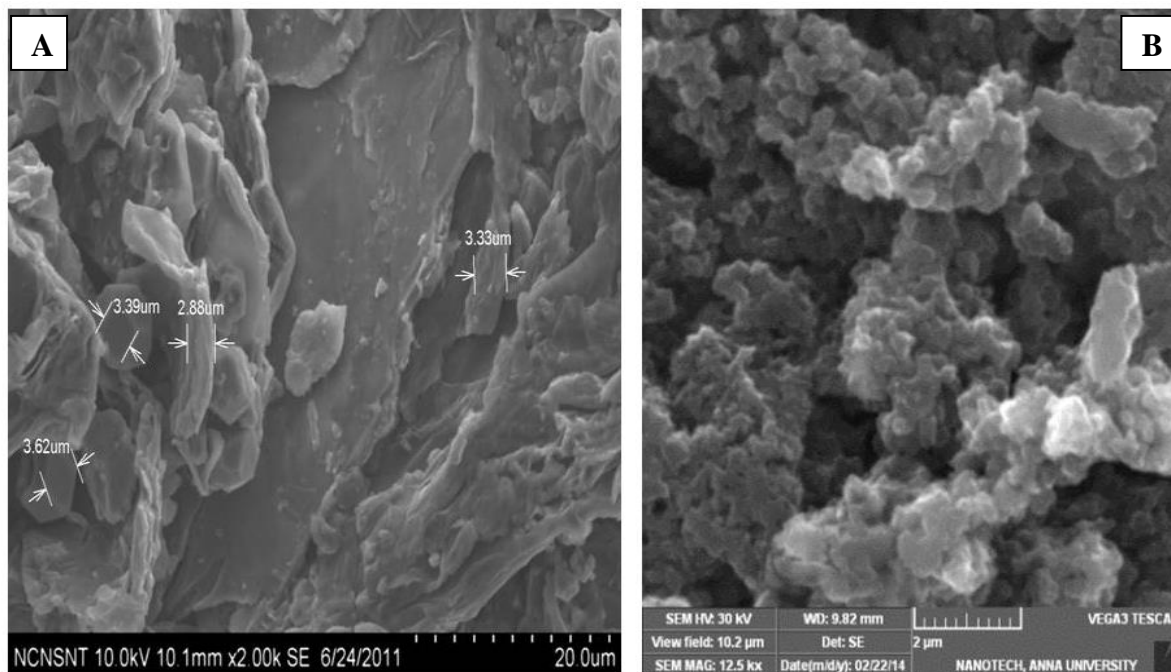


Fig .2 FE-SEM images of Graphene oxide and Graphene Oxide – Polyailine

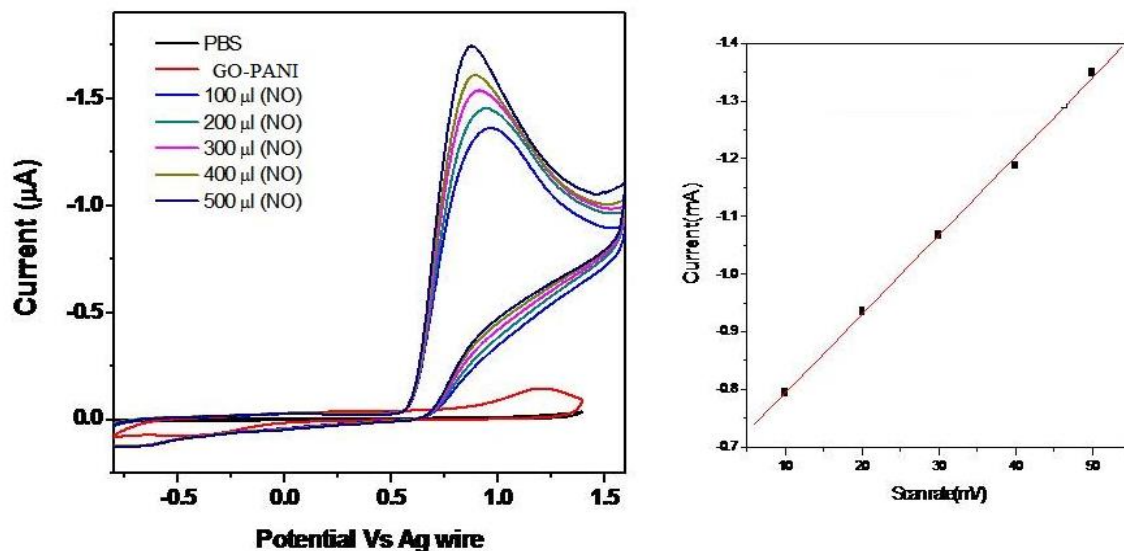


Fig .3 CVs were performed using graphene oxide-PANI for 0 mM of NO in PBS (curve 1), and 0.2 mM of NO in PBS with an graphene oxide-PANI and Ag electrode . Scan rate: 0.05 v/s B) Peak current versus scan rate plot for CVs of 0.2 mM of NO in PBS using the graphene oxide-PANI.

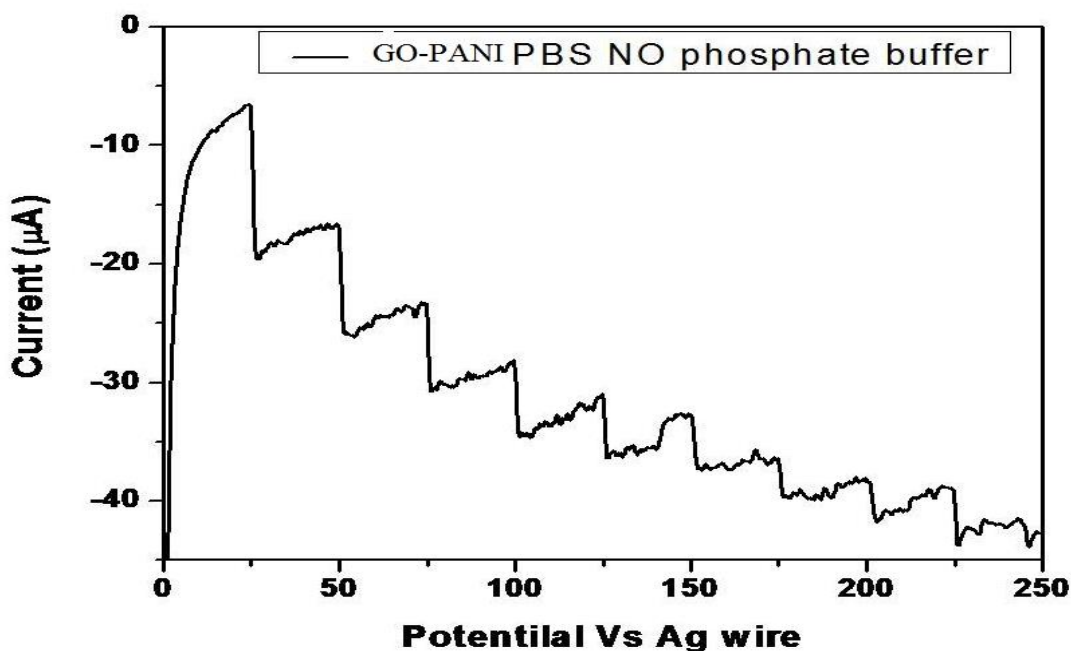


Fig .4 Amperometric action for the Nafion/PANI-GO electrode to successive infusions of NO into 10 mL of stirring 0.1 M PBS (pH 7.0) at an applied potential of +0.8 V (vs. Ag/AgCl).

References

1. Moncada, S., Palmer, R. and Higgs, E, Pharmacological Reviews, Vol. 43, No. 2, (1991), 109-142.
2. Pashai, E., Darzi, G.N., Jahanshahi, M., Yazdian, F. and Rahimnejad, M, International Journal of Biological Macromolecules, Vol. 108, (2018), 250-258.
3. Pluth, M.D., Tomat, E. and Lippard, S.J., Annual Review of Biochemistry, Vol. 80, (2011), 333-355.
4. Kavaya, R., Saluja, R., Singh, S. and Dikshit, M., Vol. 15, No. 4, (2006), 280-294.
5. Li, C.M., Zang, J., Zhan, D., Chen, W., Sun, C.Q., Teo, A.L., Chua, Y., Lee, V. and Moochhala, S, Electroanalysis, Vol. 18, No. 7, (2006), 713- 718.
6. Wink, D.A. and Mitchell, J.B., Free Radical Biology and Medicine, Vol .25 ,No. 4, (1998), 434-456.
7. Taha, Z.H., Talanta, Vol. 61, No. 1, (2003), 3-10.
8. Shibuki, K., Neuroscience Research ,Vol. 9, No. 1, (1990), 69-76.
9. Haruyama, T., Shiino, S., Yanagida, Y., Kobatake, E. and Aizawa, M, Biosensors and Bioelectronics ,Vol. 13, No. 7, (1998), 763-769.
10. Fan, C., Chen, X., Li, G., Zhu, J., Zhu, D. and Scheer, H, Physical Chemistry Chemical Physics, Vol. 2, No. 19, (2000), 4409-4413.
11. Brovkovich, V., Stolarczyk, E., Oman, J., Tombouliau, P. and Malinski, T., Journal of Pharmaceutical and Biomedical Analysis, Vol. 19, No. 1, (1999), 135-143.
12. Wen, W., Chen, W., Ren, Q.-Q., Hu, X.-Y., Xiong, H.-Y., Zhang, X.-H., Wang, S.-F. and Zhao, Y.-D., Sensors and Actuators B: Chemical, Vol. 166, (2012), 444-450.
13. Chen, D., Feng, H. and Li, J Chemical Reviews, Vol. 112, No. 11, (2012), 6027-6053.
14. Muthoosamy, K., G Bai, R. and Manickam, S, Current Drug Delivery, Vol. 11, No. 6, (2014), 701- 718.

15. Bai, R.G., Muthoosamy, K., Zhou, M., Ashokkumar, M., Huang, N.M. and Manickam, S., *Biosensors and Bioelectronics*, Vol. 87, (2017), 622- 629.
16. Ting, S.L., Guo, C.X., Leong, K.C., Kim, D.-H ,Li, C.M. and Chen, P., *Electrochimica Acta*, Vol. 111, (2013), 441-446.
17. Casero, E., Alonso, C., Vazquez, L., Petit-Domínguez, M , Parra-Alfambra, A., De La Fuente, M., Merino, P., Álvarez- García, S., De Andrés, A. and Pariente, F., *Electroanalysis*, Vol. 25 ,No. 1, (2013), 154-165.
18. Lian, W., Liu, S., Yu, J., Li, J., Cui, M., Xu, W. and Huang, J., *Biosensors and Bioelectronics*, Vol. 44, (2013), 70-76.
19. Wang, R., Yan, K., Wang, F. and Zhang, J., *Electrochimica Acta*, Vol. 121, (2014), 102-108.
20. Tan, X., Hu, Q., Wu, J., Li, X., Li, P., Yu, H., Li, X. and Lei, F., *Sensors and Actuators B: Chemical*, Vol. 220, (2015), 216-221.
21. Schoch, K., Byers, W. and Buckley, L., *Synthetic Metals*, Vol. 72, No. 1, (1995), 13-23.
22. Lin, Y. and Cui, X., *Journal of Materials Chemistry*, Vol. 16, No. 6, (2006), 585-592.
23. Batra, B., Lata, S., Rani, S. and Pundir, C., *Journal of Biomedical Nanotechnology*, Vol. 9, No. 3, (2013), 409-416.
24. Sha, R., Komori, K. and Badhulika, S., *Electrochimica Acta*, Vol. 233, (2017), 44-51.
25. Lata, S., Batra, B ,.Karwasra, N. and Pundir, C.S., *Process Biochemistry*, Vol. 47, No. 6, (2012), 992- 998.
26. Deng, X., Wang, F. and Chen, Z., *Talanta*, Vol. 82, No. 4, (2010), 1218–1224.
27. Yu, A., Liang, Z., Cho, J. and Caruso, F., *Nano Letters*, Vol. 3, No. 9, (2003), 1203-1207.
28. Singh, A., Dipak, P., Iqbal, A. *Sci Rep* **13**, 8074 (2023).
29. K. Dimyaa1 * and M. N. Potangale2 , *Journal of ISAS* , 2(1), 33-51, 2023.

Diffusion of Fe^{3+} Ions in Agar Gel Medium Containing Zinc Sulfate: Obstruction effect and Activation Energy

M. S. Gupte

Department of Chemistry, Modern College of Arts, Science and Commerce, Ganeshkhind
Pune-411053, India

Email:mohinigupte@moderncollegegk.org

Received: 13.10.23 Revised: 14.10.23,24.10.23 Accepted: 25.10.23

Abstract

The paper presents a study on the diffusion behaviour of ferric ions within an agar gel medium containing zinc sulfate electrolyte. Investigations for various aspects, including the obstruction effect introduced by the agar gel, the validation of Wang's diffusion model, and the suitability of applying transition state theory to the diffusion of Fe^{3+} ions in an agar gel medium with zinc sulfate were made. This investigation involved optimising the gel concentration, electrolyte concentration, and system temperature. The diffusion coefficients are determined by the zone diffusion technique. The results reveal that the activation energy (E) decreases as the electrolyte concentration increases, aligning with Wang's model. This decrease is attributed to the disruption of the water structure induced by ions and agar molecules. Additionally, for a fixed electrolyte concentration, the activation energy decreases with the cubic root of the weight percent of agar ($W^{1/3}$), while the diffusion coefficient (D_0) decreases with the square of the reciprocal of the weight percent of agar ($W^{-2/3}$). This behaviour is consistent with the principles of the transition state theory of diffusion.

Keywords: Diffusion, Ferric ions, Supporting electrolyte, Obstruction effect, Tracer diffusion, Transition state theory.

1.Introduction:

Diffusion is one of the most fundamental irreversible processes by which equalization of concentration is achieved by spontaneous flow of matter from higher concentration to lower concentration region regardless of gravitational forces. When an ion at very low concentration diffuses into a solution of an electrolyte with uniform composition is termed as tracer diffusion. A lot of work on diffusion of ions in various fields is being carried out in different media¹⁻⁵. The experimental methods for determination of diffusion coefficient, 'D' encounter certain difficulties in obtaining accurate data on diffusion due to turbulent flow, the very accurate control of temperature and analytical accuracy. These errors in the study of diffusion are reduced to a minimum by immobilizing the system in gel medium, which has been reported by many researchers^{6,7}. Various aspects of tracer diffusion, such as the effect of electrolyte concentration⁸, gel concentration^{9, 10} and temperature^{9, 10} in different systems have been studied and reported in a series of research papers from our laboratory. The present work deals with the effect of temperature and concentration of electrolyte on the obstruction effect for tracer diffusion of Fe³⁺ ions in zinc sulphate to confirm the Wang's model¹¹.

The study involved an investigation of these variables through the measurement of diffusion rates within a medium with gel concentrations ranging from 1.0% to 2.5%. To assess the impact of temperature on hindrance effects, diffusion coefficients for the movement of Fe³⁺ ions were determined at different temperatures, each at a concentration of 0.1 M. Additionally, studies were performed to understand the suitability of transition state theory by altering gel concentrations within a temperature range of 25°C to 45°C and maintaining a fixed concentration of ZnSO₄ at 0.1M.

2. Experimental:

The diffusion process was allowed to progress for a duration of 24 h, and we monitored the diffusion column by measuring the activity of Fe-59 at different column lengths. These measurements were carried out using a NaI (TI) detector in conjunction with a single-channel analyzer operating at 1099 keV.

In the initial series of experiments, we determined the obstruction effect and activation energy for Fe³⁺ ions in a solution of 0.1M zinc sulfate. This investigation involved different gel concentrations ranging from 1.0% to 2.5% and was carried out across a temperature range

of 25°C to 45°C. In the subsequent set of experiments, we focused on determining the activation energy for the tracer diffusion of Fe³⁺ ions in a 1% agar gel containing zinc sulfate electrolyte at concentrations ranging from 0.001 to 0.2M. This analysis was conducted over the temperature range of 25°C to 45°C. The activation energies were calculated by applying the Arrhenius equation through a least square fitting of the diffusion data, as provided below:

$$D = D_0 e^{-E/RT} \dots\dots\dots(1)$$

where E is activation energy for diffusion process and D₀ is the diffusion coefficient at very high temperature respectively.

3. Results and discussion:

3.1. Effect of gel concentration: Effect of gel on diffusion process is shown in Fig.1. As can be seen from this figure, the diffusion coefficient decreases linearly with the weight fraction of agar, which obeys the following equation ^{12,13}.

$$D_g = D_s - a\omega \dots\dots\dots(2)$$

Where D_g and D_s are diffusion coefficient in gel medium and extrapolated value of D_g to zero agar content while ‘a’ represents the slope of the plot of D_g versus ω.

The reduction in the diffusion coefficient as the concentration of gel increases (Table 1) is ascribed to the three-dimensional network formed by the larger agar macromolecules, which possess a considerably smaller diffusion coefficient due to their higher molecular weight compared to the diffusing ions. These substantial and relatively immobile macromolecules impede the movement of ions. When an ion is in close proximity to an agar molecule, it must travel along a longer path to reach the other side of the molecule. This extended diffusion path becomes more pronounced with the gel concentration increases, leading to a corresponding decrease in the diffusion coefficient.

As depicted in Fig. 1, the slope of the D_g versus ω plot decreases with an increasing concentration of electrolyte. The hindrance effect can be quantified using the parameter α, which signifies the relative reduction in the diffusion coefficient concerning the weight fraction of agar. This is calculated by dividing the slope of the plot ‘a’ by D_s. The hydration

value of agar (H), expressed as the amount of bound water in grams per gram of anhydrous agar, is determined for various systems using the following equation ¹⁴

$$\alpha = \left[\frac{1}{d_a} + \frac{H}{d_w} \right] \cdot d_w (\beta - 1) \dots\dots\dots(3)$$

where, d_a (1.6) is density of agar, d_w is the density of pure water and β (5/3) is the shape factor for agar molecules.

The values of α and H are reported in Table 2.

An examination of Table 2 reveals a consistent trend: as the concentration of the electrolyte increases, both the values of α and H decrease. This trend can be understood by considering the concept of competitive hydration between ions and agar macromolecules within a given system, and it aligns with findings from our previous reports (references ^{9, 10, 12}).

The degree of hydration of agar (referred to as H) is influenced by the presence of different ions due to the stronger attractive forces these ions exert on water molecules. In a system containing both ions and agar molecules, there exists a competition for water molecules to facilitate hydration. The extent of agar hydration is contingent on the concentration of ions in the system.

As the concentration of the electrolyte increases, there is a greater number of ions competing with agar molecules for hydration. Consequently, less water is available for the hydration of agar, leading to a reduction in the extent of agar hydration. This, in turn, results in a decrease in the value of 'H' and a decrease in the slope of Dg versus ω , indicating a reduction in Dg concerning the weight percentage of agar, as well as a decrease in $\alpha = a/D_s$ as the concentration of the electrolyte increases, as observed.

The effect of gel concentration on the activation energy required for diffusion in different systems at a specified concentration of diffusing species is investigated over the temperature range of 25-45⁰C. A plot of log D as function of 1/T is shown in Fig.2 at different gel percentages (1-2.5%) for diffusion of Fe³⁺ ions at 0.1M concentration of ZnSO₄.

As the temperature of the system rises, it becomes evident that the diffusion coefficient also increases within each system. This phenomenon can be explained by referencing the principles of the transition state theory of diffusion ^{15,16}. Since we are measuring these diffusion coefficients in an agar gel medium, it is essential to consider the influence of the

temperature on the agar gel. Nevertheless, it has been demonstrated that the obstructive impact created by the agar gel remains constant regardless of temperature variations. This finding implies that the gel's structure remains unaltered within the temperature range investigated (25°C–45°C). Consequently, alterations in temperature solely affect the diffusion process. When the temperature is elevated, a significant proportion of the diffusing particles attains the necessary energy level to surmount the potential energy barrier associated with diffusion. This results in an upward trend in the diffusion coefficient with temperature, in alignment with the principles of the transition state theory of diffusion.

Table 2 presents the activation energy (E) and D_0 values, which were determined through least squares fitting of the data using the Arrhenius equation. The standard deviation is also included. Upon examining Table 2, it becomes evident that both E and D_0 values exhibit a decline as the gel concentration within the studied system increases. This observation aligns with expectations derived from prior research on different systems and can be adequately elucidated through the framework of the transition state theory of diffusion.

The reduction in the D_0 value with increasing gel concentration suggests that the jump distance (λ) value should also decrease as gel concentration rises. Imagining a scenario of cubic packing within the liquid, one can envision a molecule oscillating around the origin with its six closest neighbours firmly positioned along the three axes. In this geometric context, each molecule is anticipated to be situated at a distance of $V^{1/3}$ from the origin, where V denotes the volume. Consequently, when considering diffusion in a single direction, the λ value is expected to vary with $V^{1/3}$, and therefore with $W^{1/3}$, where W signifies the weight percentage of agar.

Given that D_0 is directly proportional to λ^2 , it is anticipated to vary with $W^{-2/3}$. This relationship is corroborated by an observed linear association in the D_0 versus $W^{-2/3}$ plot, as illustrated in Fig.3. Moreover, the apparent pattern in the behaviour of D_0 and, consequently, gel percentage suggests that the presence of agar macromolecules inhibits longer elementary movements, allowing only shorter jumps as the gel concentration increases. This diminishing trend in activation energy with higher gel concentration aligns with this hypothesis, as depicted in Figure 4. It's worth noting that the activation energy demonstrates a linear relationship with the one-third power of gel percentage ($W^{1/3}$) in the investigated systems.

Conclusions:

Studies on effect of gel concentration on diffusion of Fe^{3+} ions in ZnSO_4 electrolyte reveals that as the concentration of the electrolyte increases, obstruction effect due to agar macromolecules measured in terms of α and extent of hydration of agar expressed in terms of H decrease. Further, Arrhenius parameters, E and D_0 decrease with increasing gel concentration ; E is found to vary with $W^{1/3}$ and D_0 with $W^{-2/3}$.

Acknowledgement: Author is thankful to Dr. Nilima Rajurkar, Former Professor and Head, Chemistry Department, SPPU for her guidance and Head, Chemistry Department, SPPU for providing the infrastructural facilities. Dr. Meera Venkatesh and Sanjay Saxena, Radiopharmaceutical Division, BARC, Mumbai are gratefully acknowledged for providing the radioisotope.

Figures

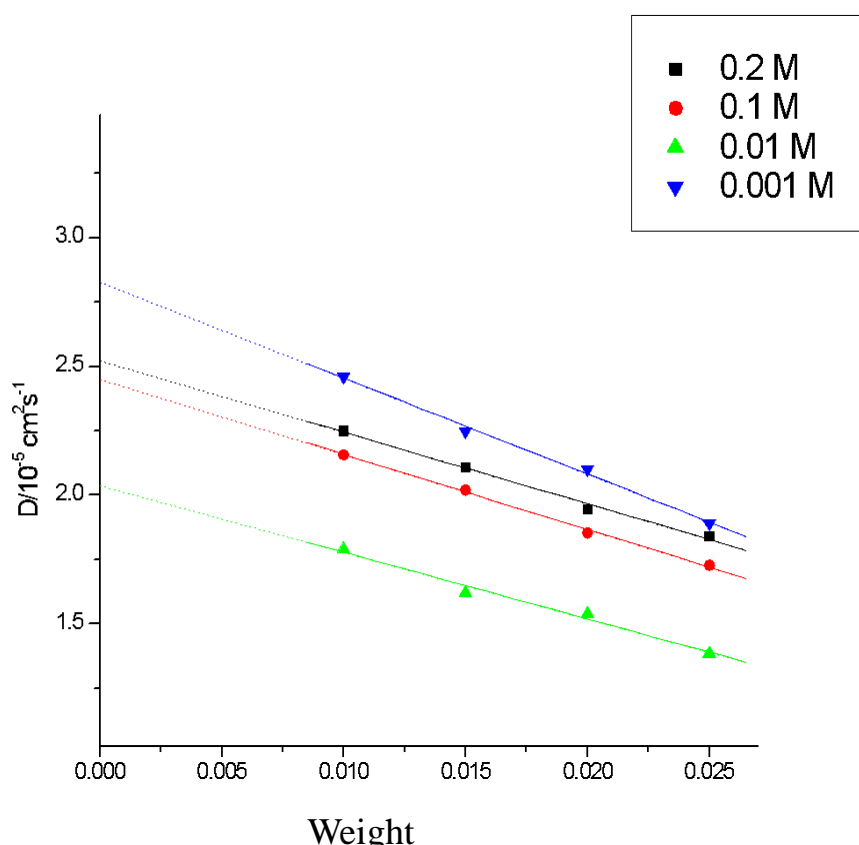


Fig.1: Obstruction effect in the tracer diffusion of Fe^{3+} ions at different concentrations of ZnSO_4 at 25°C .

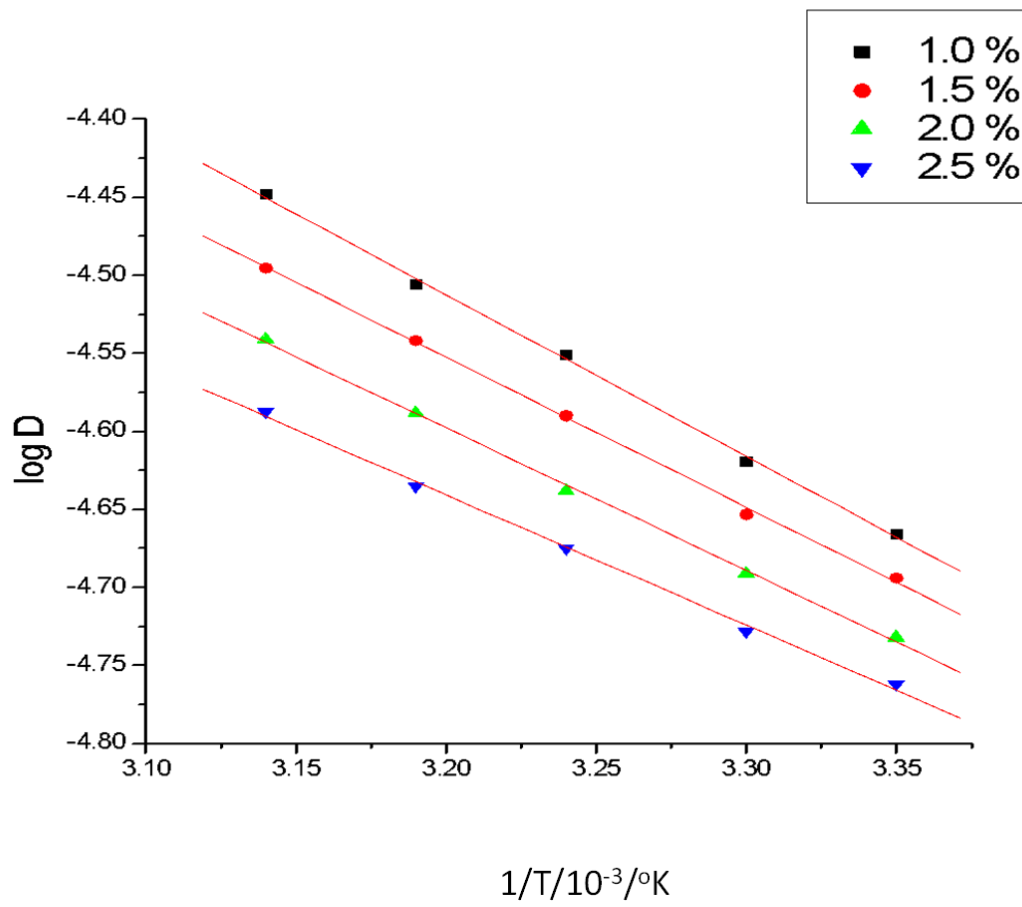


Fig.2: Activation energy for the tracer diffusion of Fe^{3+} in agar gel medium containing ZnSO_4 (0.1 M) with various gel concentrations.

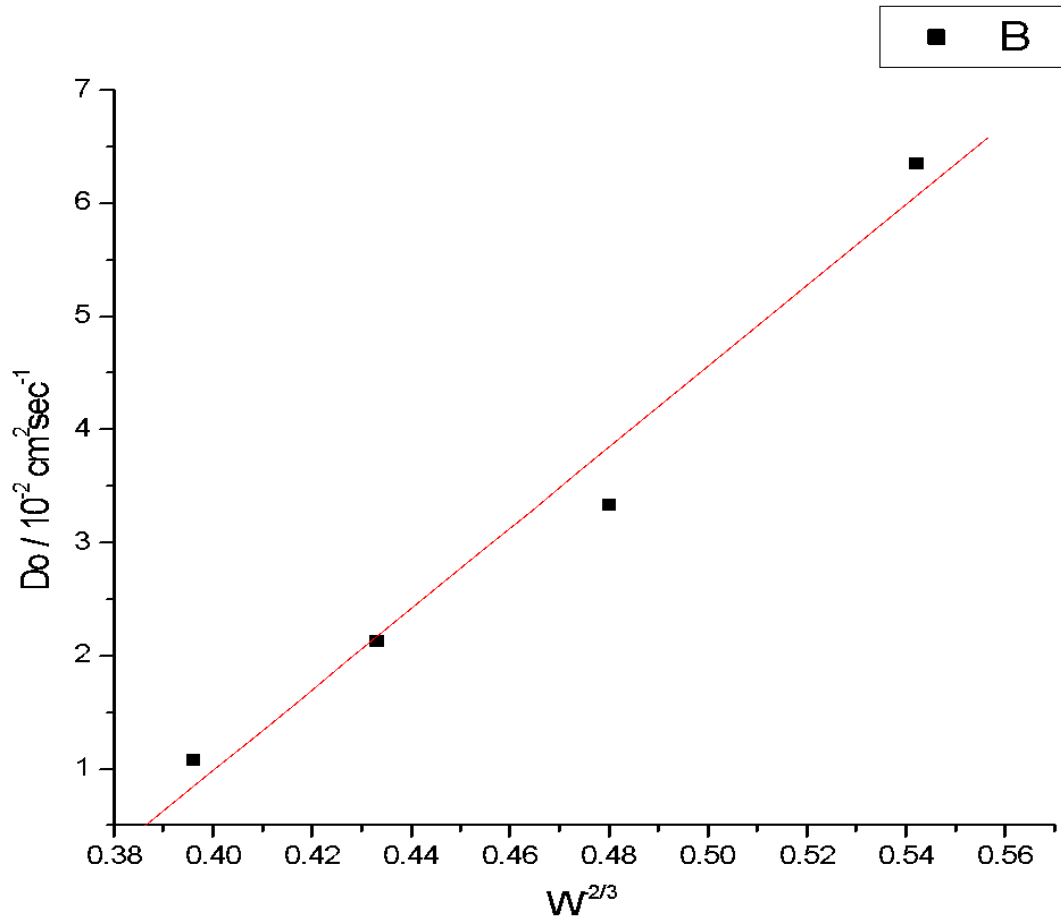


Fig.3: Variation of D_0 with $W^{-2/3}$ for tracer diffusion of Fe^{3+} ions in agar gel medium containing ZnSO_4 (0.1 M).

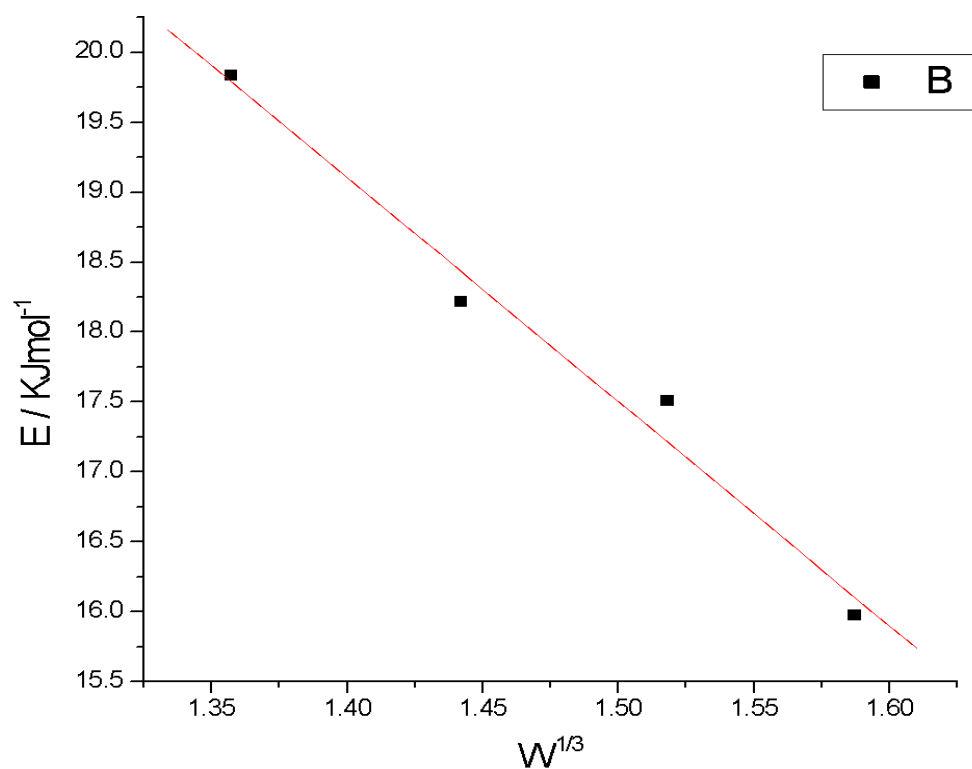


Fig.4: Variation of E with $W^{1/3}$ for tracer diffusion of Fe^{3+} ions in agar gel medium containing $ZnSO_4$ (0.1M).

Tables

Table 1: Variation of tracer diffusion coefficient of Fe⁺³ ions with weight fraction of agar at different ZnSO₄ concentrations at 25⁰ C.

ω (weight fraction) of Agar ↓	D* Fe ³⁺ / 10 ⁻⁵ cm ² s ⁻¹			
	ZnSO ₄ Concentration/M→ 0.2	0.1	0.01	0.001
0.010	2.25	2.158	1.79	2.46
0.015	2.108	2.02	1.621	2.25
0.020	1.945	1.853	1.54	2.1
0.025	1.842	1.728	1.386	1.89

Table 2: Variation of α and Hydration value of agar in terms of grams of bound water per gram of anhydrous agar for tracer diffusion of Fe⁺³ ions in ZnSO₄.

ZnSO ₄ Concentration / M	α	H
0.001	13.16	19.13
0.01	12.69	18.43
0.1	11.89	17.22
0.2	11.0	15.89

Table 3: Variation of E and Do with gel concentration for tracer diffusion of Fe⁺³ ions in ZnSO₄.

Gel percentage	E/kJmole⁻¹	Do/10⁻² cm²s⁻¹
1.0	19.84±0.4	6.36±0.021
1.5	18.40±0.3	3.34±0.010
2.0	17.51±0.3	2.13±0.006
2.5	15.98±0.4	1.08±0.004

References:

1. J. Wang, L. Zhang, J. Xue, G. Hu, *Biomicrofluidics*, 8, 024118, 2014.
2. A. Revil, D. Jougnot, *Journal of Colloid and Interface Science*, 319 (1), 226, 2008.
3. E. Quartarone, S. Davino, E. Lufrano, L. Coppola, C. Simari, and I. Nicotera*, *ChemElectroChem*,10(6),1, 2023.
4. C. Pean, B. Daffos, B. Rotenberg, P. Levitz, M. Haefele, P. Taberna, P. Simon, and M. Salanne, *Journal of the American Chemical Society*, 137 (39), 12627, 2015.
5. P. Banerjee, B. Bagchi, *J. Chem. Phy.*, 150, 190901, 2019.
6. H. J. Arnikaar and S. A. Tattithali, 21(4), 2680,1989.
7. Z. Fricke, *Electrochem.*, 31, 430, 1925.
8. N.A. Gokarn, N.S. Rajurkar, *J. Mol. Liq.* 129, 129, 2006.
9. N.S. Rajurkar, M.M. Kute, *J. Mol. Liq.* 142, 6, 2008.
10. N.S. Rajurkar, N.A. Gokarn, *J. Mol. Liq.* 122, 49, 2005.
11. J. H. Wang, *J. Am. Chem. Soc.* 74, 1182, 1952.
12. A. V. Borhade, *J. Radioanal. Nucl. Chem.* 257, 323, 2003.
13. N.S. Rajurkar, M.M. Kute, *J. Sol. Chem.*, 39, 87, 2010.
14. J.H. Wang, *J. Am. Chem. Soc.* 33, 4755, 1954.

JOURNAL OF ISAS VOLUME 2, ISSUE 2, OCTOBER 2023

15. S. Glasstone, K. J. Laidler, H. Eyring, McGraw-Hill, New York, 1941.

16. H. Eyring, J.F. Kincaid, A. E. Stearn, Chem. Rev. 28, 301, 1941.

Synthesis of Au nanospheres, Au/PVDF nanocomposites and their breath sensing properties

Amruta D. Bang¹, Parag V. Adhyapak^{1*}

¹Nanomaterials Laboratory, Centre for Materials for Electronics Technology (C-MET),(Scientific Society, Ministry of Electronics & Information Technology (MeitY), Govt. of India), Panchawati off Pashan Road, Pune 411008, Maharashtra, India

* E-mail: adhyapak@cmet.gov.in, adhyapakp@gmail.com

Received: 18.10.23 Revised: 24.10.23 Accepted: 25.10.23

Abstract

Herein, we report, a simple breath sensor based on Au/PVDF nanocomposites. Au nanostructures have been synthesized by using a simple seed mediated growth method. The synthesized Au nanostructures exhibited uniform spherical morphology with average diameter ~20 nm, confirmed by FESEM analysis. The synthesized nanostructures were further used to form nanocomposites with Polyvinylidene Fluoride (PVDF). The synthesized Au nanospheres as well as Au nanospheres/PVDF nanocomposites were tested for breath analysis. The nanocomposite materials were found to sense breath and uniform breathing patterns were generated. During breathing over sensor, voltage gets generated. The maximum voltage obtained was around 280 mV in breathing cycle.

Introduction:

Gold (Au) is a well-known noble metal with excellent optical, mechanical and electrical properties. Au exhibits various nanostructures like nanospheres^{1,2}, nanorods³⁻⁵, nanowires^{6,7}, nanoplates, nanocubes, nanostars etc. These nanostructures have vast area of applications in different fields. Some of them to list are air cleaning, emission management, water purification, power cells, and critical medical applications like anticancer therapy, drug delivery, biomarkers and biosensors applications⁸. Further, Au nanostructures have been used for composite preparation along with various polymers like polypyrene (PPy), polyaniline (Pani), polythiophene (PTh), Polyvinylidene Fluoride (PVDF), Polytetrafluoroethylene (PTFE)^{9,10} etc. These Au/Polymer nanocomposites have been used for applications such as gas sensing, humidity sensing, dielectric measurements, electrochemical supercapacitors, electrochemical sensors etc. Breath sensing and breath analysis is an emerging technology. There are many traditional breath sensing techniques like Selected Ion Flow Tube Mass Spectrometry (SIFT-MS)¹¹, Proton Transfer Reaction Mass

Spectrometry (PTRMS)¹², Gas Chromatography Mass Spectrometry (GC-MS)¹³ which are non-invasive as well as highly sensitive. However, all these methods have drawbacks like huge set up, complex machineries and expensive. Nowadays many reports are coming up with various nanostructure based electrical and optical sensors for breath analysis¹⁴⁻¹⁶. Feiyi Liao et.al¹⁵ have developed a breath sensor to detect apnea syndrome by transfer-printing vanadium dioxide (VO₂) thin films on PDMS substrates. They have obtained the response time and recovery time of 0.5 s. Seon Jin Choi et.al¹⁶ have synthesized WO₃ hemitube nanostructure assisted by O₂ plasma surface modification with functionalization of graphene-based material for the detection of acetone (CH₃COCH₃) and hydrogen sulfide (H₂S) which are biomarkers for the diagnosis of diabetes and halitosis, respectively. They have showcased response times of 11.5 ± 2.5 s and 13.5 ± 3.4 s to 1 ppm acetone as well as 12.5 ± 1.9 s and 10.0 ± 1.6 s to 1 ppm of H₂S, respectively. Danling Wang et al¹⁷ have synthesized novel nanostructured K₂W₇O₂₂ and tested on its feasibility for acetone detection in breath with response time of 12 s is achieved. In Our earlier reports we have synthesised Au nanowires and nanorods based nanocomposites^{3,6}. They are proved to be excellent humidity sensors and have good sensitivity towards human breath. In the same regard, here, we report breath analyzer based on Au nanospheres and PVDF nanocomposite.

Experimental:

Synthesis of Au nanospheres:

Au nanospheres have been synthesized using earlier reported method^{1,2}. The detailed procedure is as follows. Gold chloride trihydrate (HAuCl₄.3H₂O, 99%) (Sigma Aldrich) and trisodium citrate dihydrate (Na₃C₆H₅O₇.2H₂O, 99 %) (Alfa Aesar) were used as a precursor. For the synthesis of seed solution, 150 mL of 2.2 mM trisodium citrate dihydrate (TSC) was dissolved in DI water and heated at ~100 °C in a 250 mL three necked round bottom flask with a condenser. The solution was stirred continuously. 1 mL of 25 mM HAuCl₄ was added to the boiling TSC solution. The color changes to light pink after 15 – 20 min, indicating formation of Au seeds. The solution was allowed to cool down to 90°C, then to this solution, further, 1mL of 60 mM TSC was added followed by addition of 1 mL of 25 mM HAuCl₄ after 2 min. The reaction mixture was continued to heat with stirring for 30 mins and again TSC and HAuCl₄ were added and kept under same condition for 30 mins. Then the solution was allowed to cool down to room temperature.

Synthesis of Au nanosphere/ PVDF nanocomposite

Various concentrations of PVDF (0.5, 1, 2, 5 wt%) were prepared in DMF and 1 mL as-prepared Au nanosphere solution was added to this PVDF/DMF solution. This nanocomposite mixture was stirred for 1 h at 60°C. The resultant as synthesized Au nanosphere solution and nanocomposite solution was used as it is for UV-Visible Spectroscopic and FTIR analysis. The nanocomposite solution was coated on glass slide to form a film for XRD and on interdigitated electrode for breath sensing analysis.

Characterizations:

(a) Physiochemical Characterization of the as prepared composites.

Fourier-transform infrared spectroscopy (FTIR) analysis was done using a Bruker TENSOR37 spectrometer, X-Ray Diffraction analysis is done on a Rigaku Miniflex diffractometer using CuK α radiation ($\lambda = 1.5405 \text{ \AA}$; nickel filter). Optical absorption spectra were recorded on a Hitachi UV-Visible Spectrophotometer (model U-3210). Morphological studies were conducted using FE-SEM (Hitachi Model 5890). For the characterization, the samples were prepared by drop casting the material on alumina stub.

(b) Breath – Sensing Characterization.

The breath sensing experiments were conducted for Au nanospheres and Au/PVDF nanocomposite as shown in schematic Fig. 1. For this purpose, the material was dropcasted on an alumina substrate having silver interdigitated electrodes printed on it. Once the material is coated on the substrate, it is allowed to dry in an oven @ 120 °C for 1 h. Using this material coated IDE, the breathing tests were carried out. The change in voltage with respect to breathing was recorded on Digital multimeter (Keithley DMM 7510).

Results and discussion:

Polyvinylidene fluoride (PVDF) $(-\text{CH}_2-\text{CF}_2)_n$ is a semi crystalline polymer. There are 3 polymorphs of PVDF viz α , β and γ . Among these, β phased PVDF¹⁸⁻²⁰ is desirable due to its ferroelectric nature. The formation of β phase was first confirmed from the FTIR analysis. The FTIR spectra of the as prepared Au nanospheres, PVDF and Au / PVDF nanocomposite are shown in Fig 2. From the FTIR spectra of nanocomposite, absorption bands at 410, 478,

510, 876, 1071, 1275, 1402, 1433 related to β phase are observed. Addition of Au nanospheres to PVDF have helped in the β phase formation of the material^{3,21}.

The XRD patterns of pure PVDF powder, PVDF film drop casted on glass slide and Au/PVDF nanocomposite is presented in Fig 3. Fig 3 (a) exhibits the XRD pattern of PVDF powder. PVDF powder is mainly made up of α - phase. It could be confirmed from the two intensive peaks at 18.34° and 19.90° and a minor peak at 26.66° corresponding to (020), (110) and (021) reflections of monoclinic α – phase crystals. When the film of PVDF was prepared (Fig. 3(b)), the pattern clearly exhibit the semi crystalline nature of the sample in the view of the broad peak within the range of 15 to $22^\circ 2\theta$. Crystalline planes at $2\theta = 18.43^\circ$, 20.02° , 26.98° , 32.47° , 36.07° , 38.62° are indexed as (020), (110), (021), (121), (200), (131), respectively and it is consistent with β – phase (JCPDS Card No: 42 – 1650). The ferroelectric β phase is characterized by an all – trans (TTTT) conformation. The peak at 18.43° is very minor confirming the formation of β phase. The heat treatment was given to PVDF to obtain the β phase. For Au / PVDF nanocomposite the peaks around 18° are broad and minorly present indicating formation of both β and γ phase²¹.

Fig. 4 (a) depicts the UV-Vis spectrum of Au/PVDF nanocomposite. Here both the signature peaks of PVDF (observed at 240 nm and 278 nm) as well as Au nanosphere (observed at 522 nm) could be observed in the UV-Vis spectrum of nanocomposite. The PVDF peaks in nanocomposite are observed to be slightly blue shifted than pristine PVDF film which confirms the formation of Au/PVDF nanocomposite³. In pristine PVDF film (Fig. 4 (b)) two signature peaks at 242 nm and 292 nm are observed. Whereas, optical absorption spectrum of Au nanosphere (Fig. 4 (c)) exhibited surface plasmon resonance (SPR) peak²²⁻²⁴ at around 522 nm confirming the formation of Au nanospheres.

The FESEM images of Au nanospheres, pristine PVDF and PVDF/Au nanosphere composite are as shown in Fig. 5(a), (b) and (c) respectively. From the Fig 5 (a) uniform sized Au nanoparticles with more or less spherical shape are observed. The size of the Au nanoparticles is ~ 20 nm in diameter. Fig.5 (b) depicts the FESEM image of PVDF matrix which shows the smooth porous structure of the polymer. In case of Au/PVDF nanocomposite (Fig. 5(c)) this smooth polymer structure was found to be disintegrated probably due to incorporation of Au nanospheres inside polymer matrix²¹. Moreover, due to nano size (~ 20 nm), it is difficult to spot the Au nanospheres in FESEM.

Further, these Au nanospheres and Au/PVDF nanocomposites were tested for breath sensing analysis. As reported earlier, Au nanostructures are excellent humidity sensing materials^{6,25} and can also be sensitive towards human breath³ since human breath contains 90% humidity. For the breath sensing tests, the breath samples of a 34 years old female have been used. When tested for breath exposure, our materials exhibited change in resistance and also change in voltage. The resultant waveforms pertaining to change in voltage were recorded for normal breathing with nose and forced breathing with mouth. Fig. 6 (a) shows the change in voltage of Au nanospheres for normal breath-in and breath-out. The pattern is uniform and the peaks are Sharpe showing good sensitivity of Au nanospheres towards breath. Fig. 6 (b) shows the change in voltage of the Au nanosphere after the forced inhale and exhale of breath on the material. It is observed that ~200 mV voltage is generated in the material. Also, the response to breath is uniform, showing good sensitivity of the material towards breath. The sensor response was studied over a period of 6 months, and found to be stable. Fig. 7 (a) and (b) shows the normal breathing pattern and forced exhale pattern of Au/PVDF nanocomposite. Here, from the generated patterns, it could be observed that there is storage of charge with each breath in case of normal breathing pattern. Here PVDF plays an important role in charge storage which is not the case with normal breathing pattern of Au nanosphere. From the Fig. 7 (b) the Au/PVDF nanocomposite has generated a voltage of 250 mV which is higher than that of Au nanospheres. Thus Au/PVDF nanocomposite is excellent material for breath analysis and its property of charge generation and storage can be useful to fabricate self-powered device.

Mechanism of breath sensing:

The breath sensing mechanism can be explained on the basis of Grotthus chain mechanism²⁶. Grotthus chain mechanism is based on the absorption of moisture on the material surface and in turn, change in the electrical properties. It is well known that, breath contains 90% of humidity. Here, the Au surface chemisorbed water molecule, on exposure to breath, forming hydroxyl species. With increase in humidity, the process of physisorption initiated through hydrogen bonding on previously chemisorbed hydroxyl species. The process of physisorption continues as humidity increases further. Hopping of protons between the hydroxyl groups forms series of dipoles which can conduct charge easily. Therefore, there is sharp change of conductance/resistance and consequent high sensitivity in this region. If the humidity increases further, number of layers of hydroxyl group being adsorbed increases, resulting in weak electrostatic force between the chemisorbed layer and the physisorbed layer. hence,

less hydronium ions are released, and small change is detected in the resistance resulting in decreased sensitivity in higher humidity conditions.

Conclusions:

Au nanospheres and their composite with PVDF have been synthesized successfully. Here quasi spherical shaped Au nanoparticles have obtained with an average diameter of 20 nm. The XRD and UV-Vis spectrum of the Au/PVDF nanocomposite have confirmed the presence of Au nanoparticles in PVDF matrix. The FTIR spectrum of the nanocomposite shows the presence of β phase PVDF in the nanocomposite. All the synthesized composites were tested for breath sensing. The Au/PVDF nanocomposite with 2 wt % PVDF has shown excellent sensitivity towards breath and has generated a voltage of 280 mV, just by breathing on it.

Acknowledgment

This work was supported by the Kiran Division of the Department of Science and Technology through the Women Scientist Scheme (WOS-A) under Grant SR/WOS-A/PM-72/2019. Amruta Bang is thankful to the "Women Scientists Scheme (WOS-A)" for the financial support.

Figures:

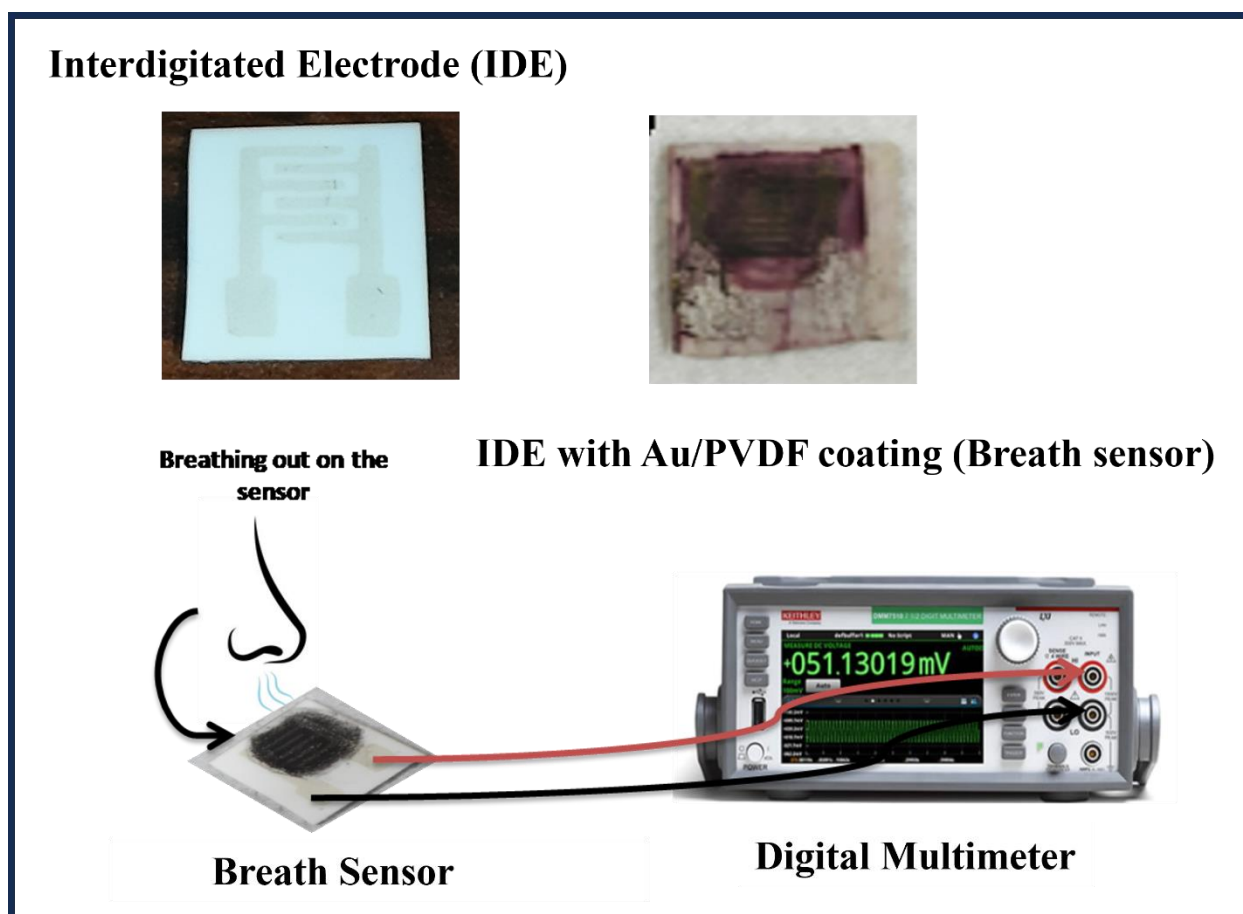


Fig. 1. Breath sensing set up.

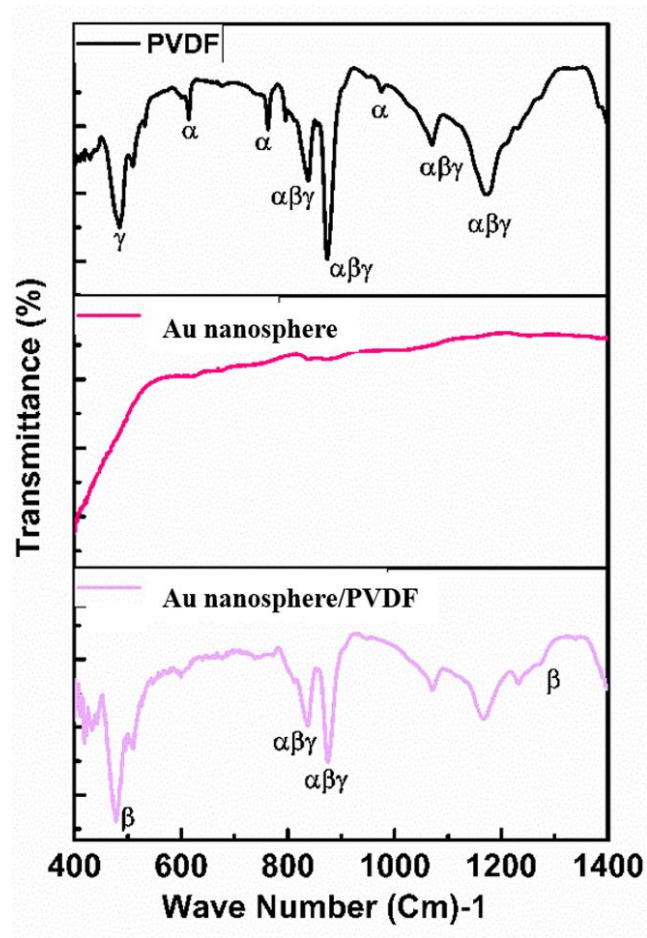


Fig. 2. FTIR spectrum of PVDF, Au nanosphere & PVDF/Au nanosphere nanocomposite.

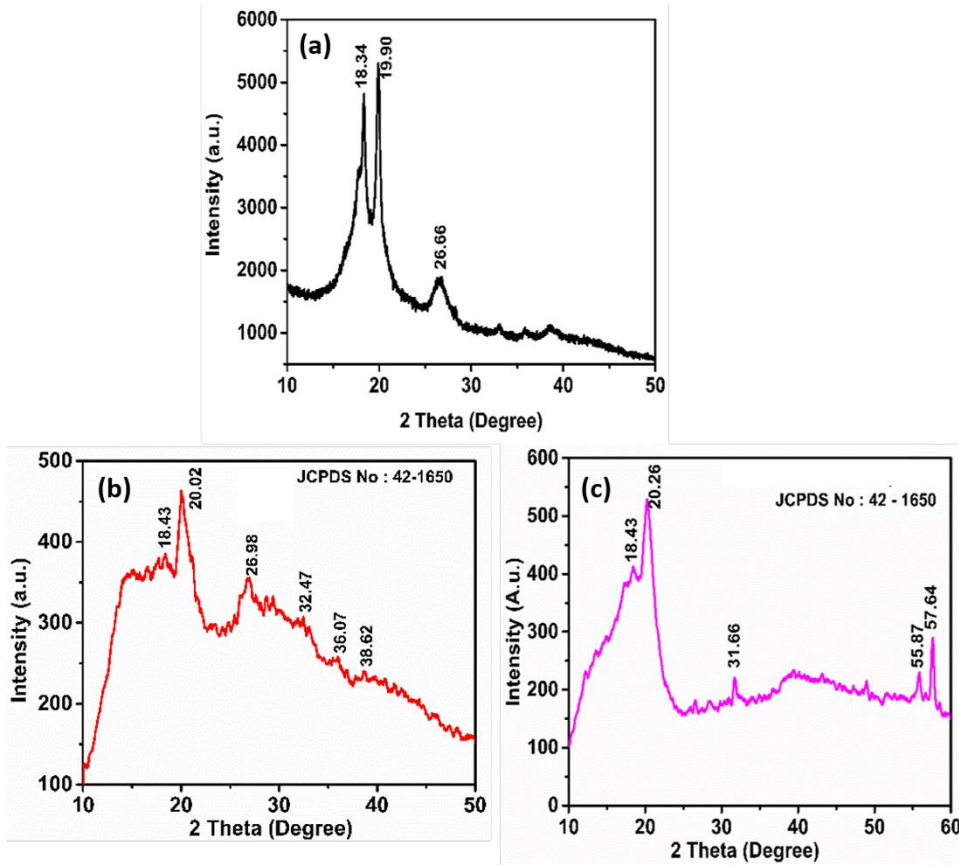


Fig. 3 (a) XRD spectrum of PVDF/DMF solution casted on glass slide. (b) XRD spectrum of PVDF powder. (c) XRD spectrum of PVDF/Au nanosphere nanocomposite

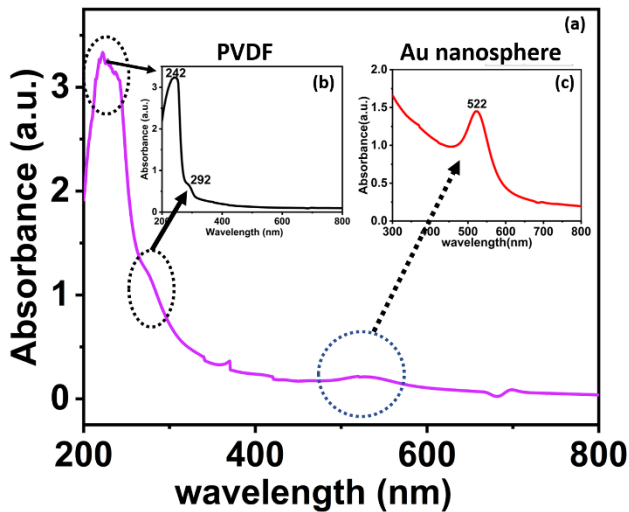


Fig.4. (a) UV Visible spectrum of Au/PVDF nanocomposite, inset: (b) PVDF film. (c) Au nanosphere

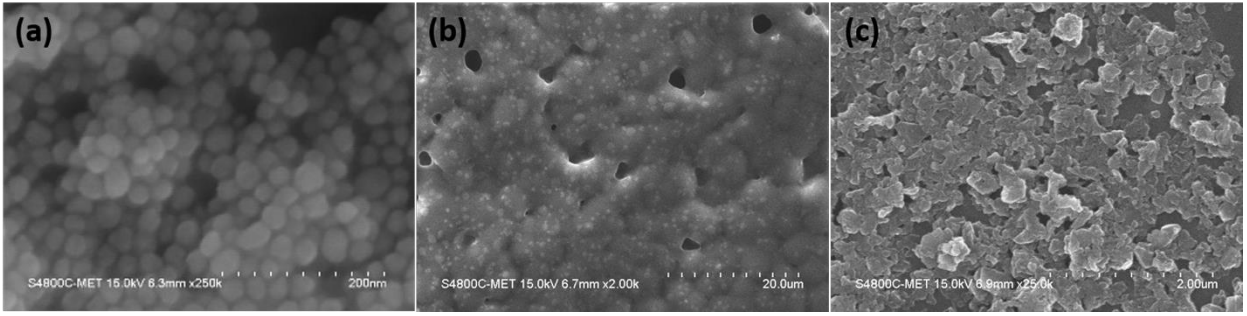


Fig. 5. FESEM images of (a) Au nanospheres (b) PVDF (c) Au nanosphere/PVDF composite

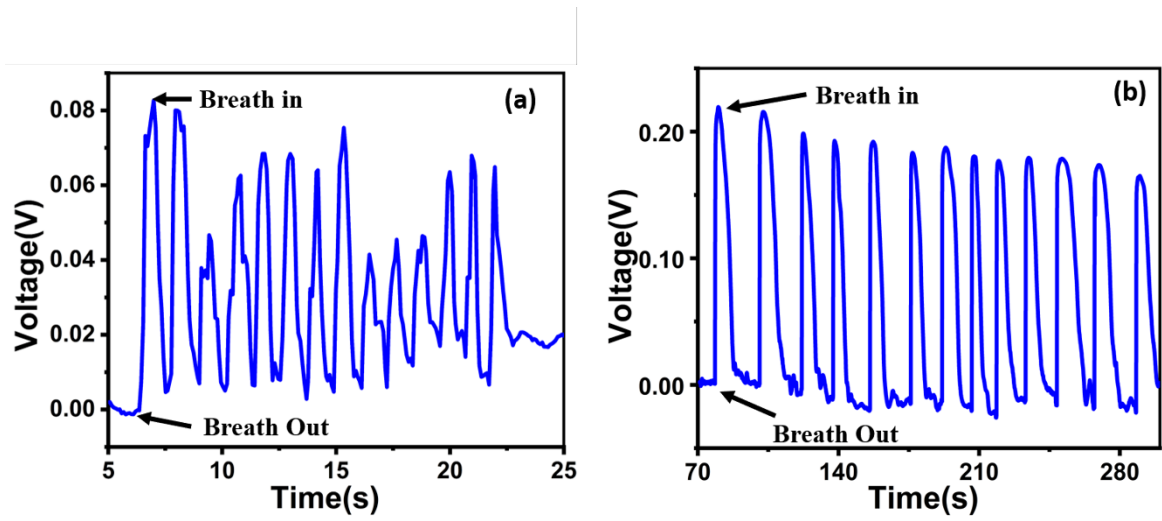


Fig. 6. (a) Normal breathing pattern (with nose) (b) forced exhale pattern (with mouth) for Au nanospheres

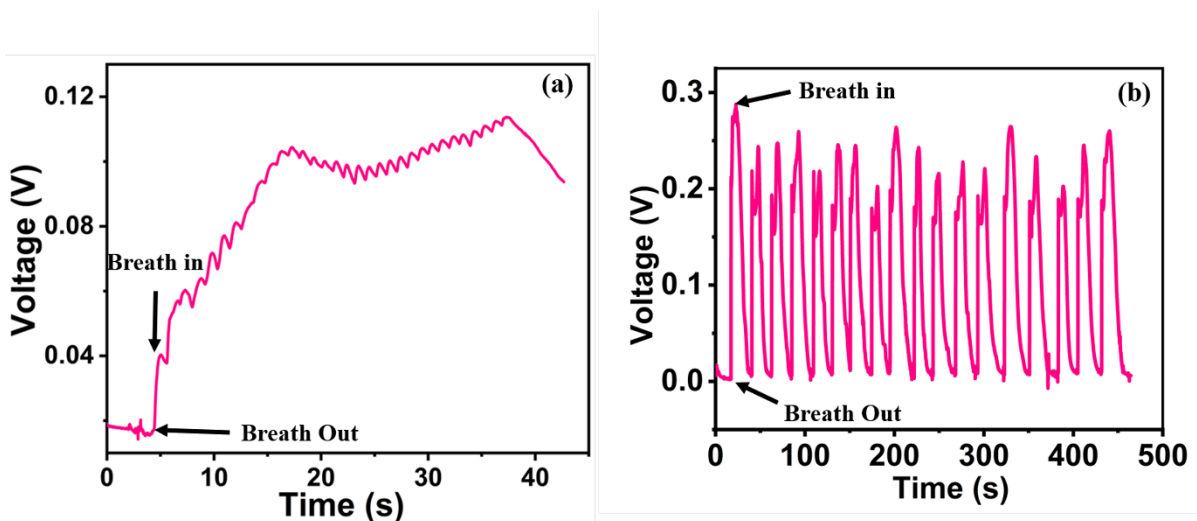


Fig. 7. (a) Normal breathing pattern (with nose) (b) forced exhale pattern (with mouth) for Au/PVDF nanocomposite

References

1. Bastús, Neus G., Joan Comenge, and Víctor Puntès. *Langmuir* 27, no.17:11098-11105 (2011).
2. Vished Kumar, Vithoba Patil, Amey Apte, Namdev Harale, Pramod Patil, and Sulabha Kulkarni. *Langmuir* 31, no. 48: 13247-13256 (2015).
3. Amruta D. Bang, Monika Ghalawat, Pankaj Poddar, Sulabha K. Kulkarni, and Parag V. Adhyapak. *IEEE Sensors Journal* 23, no. 7:6473-6480 (2023).
4. Amey Apte, Prashant Bhaskar, Raja Das, Smita Chaturvedi, Pankaj Poddar, and Sulabha Kulkarni. *Nano Research* 8, no. 3: 907-919 (2015).
5. B. Nikoobakht, and El-Sayed, M.A.,. *Chemistry of Material* 15(10), pp.1957-1962(2003).
6. Parag V. Adhyapak, Aishwarya M. Kasabe, Amruta D. Bang, Jalindar Ambekar, and Sulabha K. Kulkarni. *RSC advances* 12, no. 2: 1157-1164 (2022).
7. X. Jiang, X. Qiu, Fu, G., Sun, J., Huang, Z., Sun, D., Xu, L., Zhou, J. and Tang, Y., *Journal of Materials Chemistry A*, 6(36), pp.17682-17687(2018).
8. Ines Hammami and Nadiyah M. Alabdallah. *Journal of king Saud university-science* 33, no. 7: 101560(2021).
9. Viruntachar Kruefu, Anurat Wisitsoraat, Adisorn Tuantranont, and Sukon Phanichphant. *Nanoscale Research Letters* 9: 1-12. (2014)
10. Manojit Pusty, Lichchhavi Sinha, and Parasharam M. Shirage. *New Journal of Chemistry* 43, no. 1: 284-294 (2019).
11. [11] David Smith and Patrik Španěl. *International Reviews in Physical Chemistry* 15, no. 1: 231-271(1996).
12. A. Jordan, A. Hansel, R. Holzinger, and W. Lindinger. *International Journal of Mass Spectrometry and Ion Processes* 148, no. 1-2: L1-L3(1995).
13. Michael Phillips, Kevin Gleeson, J. Michael B. Hughes, Joel Greenberg, Renee N. Cataneo, Leigh Baker, and W. Patrick McVay. *The Lancet* 353, no. 9168: 1930-1933. (1999)
14. [14] Xinyuan Zhou, Zhenjie Xue, Xiangyu Chen, Chuanhui Huang, Wanqiao Bai, Zhili Lu, and Tie Wang. *Journal of materials chemistry B* 8, no. 16: 3231-3248 (2020).
15. Feiyi Liao, Zheng Zhu, Zhuocheng Yan, Guang Yao, Zhenlong Huang, Min Gao, Taisong Pan et al. *Journal of breath research* 11, no. 3: 036002 (2017).

16. Seon-Jin Choi, Franz Fuchs, Renaud Demadrille, Benjamin Grévin, Bong-Hoon Jang, Seo-Jin Lee, Jong-Heun Lee, Harry L. Tuller, and Il-Doo Kim. *ACS applied materials & interfaces* 6, no. 12: 9061-9070 (2014).
17. D. Wang, Q. Zhang, M.R. Hossain, and M. Johnson, *IEEE Sensors Journal*, 18(11), pp.4399-4404. 2018
18. Xiaomei Cai, Tingping Lei, Daoheng Sun, and Liwei Lin. *RSC advances* 7, no. 25: 15382-15389. (2017)
19. Jianwen Zhang, Peng Cao, Zhaoliang Cui, Qian Wang, Fan Fan, Minghui Qiu, Xiaozu Wang, Zhaohui Wang, and Yong Wang. *AIP Advances* 9, no. 11 (2019): 115219.
20. O. García-Zaldívar, T. Escamilla-Díaz, M. Ramírez-Cardona, M. A. Hernández-Landaverde, R. Ramírez-Bon, J. M. Yañez-Limón, and F. Calderón-Piñar. *Scientific reports* 7, no. 1: 1-8(2017).
21. Yasin Orooji, Babak Jaleh, Fatemeh Homayouni, Parisa Fakhri, Mohammad Kashfi, Mohammad Javad Torkamany, and Ali Akbar Yousefi. *Polymers* 12, no. 11: 2630(2020).
22. Maier, A. Stefan, In *Plasmonics: fundamentals and applications*, pp. 65-88. Springer, New York, NY, 2007.
23. Amendola, Vincenzo, Moreno Meneghetti, Mauro Stener, Yan Guo, Shaowei Chen, Patricia Crespo, Miguel Angel García, Antonio Hernando, Paolo Pengo, and Lucia Pasquato. In *Comprehensive analytical chemistry*, vol. 66, pp. 81-152. Elsevier, 2014.
24. Vivek Garg, Brajendra S. Sengar, Vishnu Awasthi, Pankaj Sharma, C. Mukherjee, Shailendra Kumar, and Shaibal Mukherjee. *RSC advances* 6, no. 31: 26216-26226 (2016).
25. Parag Adhyapak, Rohini Aiyer, Sreekantha Reddy Dugasani, Hyeong-U. Kim, Chung Kil Song, Ajayan Vinu, Venkatesan Renugopalakrishnan, *Royal Society Open Science* 5, no. 6: 171986. (2018)
26. N. Agmon, *Chemical Physics Letters*, 244(56), pp.456-462. 1995.

Effect of addition of fillers on Cellulose/ β -TCP polymer Composites: Thermal, Mechanical and Antimicrobial Properties

T. S. Kiruthika¹, B. Deepan Kumar^{1,2} and V. Jaisankar^{1*}

¹PG and Research Department of Chemistry, Presidency College (Autonomous),
Chennai-600 005, Tamil Nadu, India.

²Department of Chemistry, Institute of Chemical Technology, Tharamani,
Chennai-600 113, Tamil Nadu, India.

*Email: vjaisankar@gmail.com

Received: 13.7.23 Revised: 25.8.23, 28.8.23, 28.10.23 Accepted: 28.10.23

Abstract

Cellulose-based polymeric composites have received considerable attention as appealing biomimetic alternatives for a variety of biological applications because of their unique mechanical characteristics and appreciable bioactivity. In this investigation, four ternary polymeric composites were prepared, with cellulose serving as a typical common biopolymer and β -tricalcium phosphate (β -TCP) serving as a common bioceramic component. The naturally available hemp was used for the isolation of cellulose. The solution precipitation process was used to create the bioceramic substance β -TCP. Cellulose/Agar-Agar (AA)/ β -TCP, Cellulose/I-Carrageenan (CC)/ β -TCP, Cellulose/Polyvinyl alcohol (PVA)/ β -TCP, and Cellulose/Polyvinylpyrrolidone (PVP)/ β -TCP were the four polymeric composites prepared. The thermal and mechanical properties of the prepared composites were analysed and were compared. The SEM images of these materials indicated that the presence of β -TCP in the composites reveals notable morphological changes in the surface that are appropriate for the cell adhesion nature. The antimicrobial properties such as antibacterial, antifungal, anticancer and *in vitro* wound healing ability of the prepared composites open a new perspective in the applications for biomaterials field.

Key words: cellulose, hemp, mechanical, bioceramic, *in vitro*, wound healing.

1 Introduction

Polymer matrix composites (PMCs) have recently received a lot of attention in the scientific community due to their outstanding features that make them ideal for a wide range of technical applications. It is well recognized that composite materials are more affordable, easier to produce, and have improved strength and durability^{1,2}. Due to the wide range of features of PMCs, current research focuses primarily on the production of PMCs reinforced with fibres (either natural or synthetic) and fillers (either organic or inorganic). Particularly,

synthetic fibres are mainly favoured in marine, automotive, aerospace, and construction applications because of their better strength, heat retention, durability, performance with lightweight materials, cheap investment requirements, and capacity to manufacture any complex structure. In addition, natural fiber-reinforced polymer composites (FRP) are most frequently created and employed in a variety of structural and non-structural applications with low to medium loads. Natural fibre composites are light in weight, entirely recyclable, renewable, and sustainable. They also have cheap extraction and processing costs. Fibre content, fibre orientation, fibre size, and fibre placement are only a few of the factors that affect how natural fibre composites behave^{3,4}. However, some flaws in natural and synthetic fibres meant that the obtained composites' qualities did not match what was anticipated. As a result, researchers discovered numerous strategies for enhancing the characteristics of FRPs. Generally speaking, two frequently used techniques (reinforcement of FRP and Hybridisation of FRP²⁶) are used to enhance the mechanical, physical, thermal, tribological, and optical properties of FRPs.

The process of hybridising a composite involves combining FRPs with different kinds of natural or synthetic fibres or fillers to create composites that have the combined qualities of the two materials and may be used in a wider range of applications. If the fibres are hybridised, there are a variety of techniques one can use, such as layer-by-layer stacking, placing various fibres in a single layer, changing the orientation of the fibres, and placing only certain fibres in a layer. By including nanofillers, hybridization can be accomplished even at the nanoscale, producing hybrid nanocomposites^{5,6}. The type of nanofiller used, how it was made, how it was dispersed, and how the fillers interacted with the fibres and matrix all affected the properties of hybrid nanocomposites. The incorporation of filler materials into a polymer matrix or FRPs is a frequent study topic pursued by a variety of researchers. Filler materials are typically added to FRPs to enhance the material performance by enhancing the physical and mechanical properties of the composites. They are generally thought of as inert materials. Fillers provide composites a better surface quality and delay the development of coarse structure, resulting in improved mechanical qualities that are hard to achieve with coarse structure^{7,8}. Either organic or inorganic materials are used as fillers. To achieve improved thermal stability, tribological behaviour, good interfacial features, and higher mechanical qualities, inorganic fillers are utilized in polymer composites.

2 Experimental

2.1 Materials and Methods

The chemicals used in the isolation of cellulose and carboxymethyl cellulose were Sodium hydroxide, Hydrogen peroxide, sodium metabisulphide, Glacial acetic acid, Ethanol, Hydrochloric acid, Monochloroacetic acid and Methanol were purchased from Alfa Aesar. The chemicals used for the preparation of bioceramics β -Tricalcium phosphate were Calcium nitrate tetrahydrate (CNT), Phosphoric acid, Ammonia, Potassium dihydrogen phosphate and were purchased from Alfa Aesar^{17,18}. All the aqueous solutions used in the preparation were made with distilled water. The Analar grade solvents used in the investigation were purchased from Merck.

2.2 Isolation of Cellulose from hemp

The cellulose has been isolated from various plant sources namely hemp, jack fruit peel, pineapple leaves and corn cobs. The yield of cellulose isolated from hemp was high and possess optimal physico-chemical properties¹⁹. Hence, it is chosen for the preparation of cellulose composites, characterisation and biomedical applications.

2.3 Synthesis of β -Tricalcium phosphate

In the preparation, Calcium nitrate tetrahydrate (CNT) and Potassium dihydrogen phosphate were used as calcium and phosphorous precursors respectively. Aqueous solution of 1M calcium nitrate tetrahydrate and 0.67M potassium dihydrogen phosphate were prepared²⁰. The prepared CNT solution was added slowly drop wise in a beaker containing potassium dihydrogen phosphate. Ammonia was added to maintain the pH 11 during the reaction and was kept in magnetic stirring for 1 h. Gelation started to occur and was kept aging for 24 h. The resulting filtrate was then rinsed with distilled water and was then subjected to calcination at 1000 °C for 30 min.

2.4 Preparation of polymer composites

The polymeric composite composed of cellulose/Agar-Agar (AA)/ β -TCP was prepared by solution casting method. The stoichiometric ratio of Cellulose:AA: β -TCP taken was 5:4:1 for the preparation. Initially, cellulose from hemp and Agar-Agar were dissolved in hot water separately and were mixed²⁴. Then the mixture was stirred for about few hours. To this

desired amount of β -TCP powder, dissolved in distilled water was added. The mixture was stirred vigorously for 2 h and was cast on a teflon petri dish and was dried in an oven. Similarly, the polymer composites cellulose/AA/ β -TCP, cellulose/CA/ β -TCP, Cellulose/PVA/ β -TCP and cellulose/PVP/ β -TCP were also prepared.

3 Results and Discussion

The β -TCP integrated cellulose composites were characterized by the following analytical techniques.

3.1 FTIR Spectral Analysis

The FTIR spectra for β -TCP, cellulose/AA/ β -TCP, cellulose/CA/ β -TCP, cellulose/PVA/ β -TCP and cellulose/PVP/ β -TCP are shown in Fig I. For β -TCP, the prominent absorption bands at 3443 and 1638 cm^{-1} are ascribed to adsorbed water^{22, 23}. The PO_4^{3-} group is stretched in the bands at 900-1200 cm^{-1} ^{22,23}. The vibration peaks of PO_4^{3-} in β -TCP are shown by the strong peaks at 561 cm^{-1} and 607 cm^{-1} .

The IR absorption peaks for composites show the peak at 3429 cm^{-1} is for the OH stretching vibration whereas the peak at 2921 cm^{-1} is connected with methoxyl groups. The peak at 2852 cm^{-1} is for the CH_2 bending vibration. The peak at 1633 cm^{-1} corresponds to the surface adsorbed water molecule. The peak at 1025 cm^{-1} is corresponds for the OH bending vibration and the peak at 847 cm^{-1} is for 3,6-anhydro-galactose bridges. The peaks at 562 cm^{-1} and 617 cm^{-1} is for the PO_4^{3-} groups in β -TCP. The peak at 2920 cm^{-1} corresponds to the stretching vibration of C-H group. The peak at 1731 cm^{-1} is for the C=O stretching vibration. The peak at 1428 cm^{-1} is for the CH_2 bending of pyranose ring. The peaks around 900 cm^{-1} - 1200 cm^{-1} is for the stretching mode of PO_4^{3-} . The peak at 1141 cm^{-1} is for the C-O-C stretching vibration. The peak at 670 cm^{-1} corresponds to the PO_4^{3-} vibration of tricalcium phosphate. The peak at 2919 cm^{-1} is for the Asymmetric stretching of pyrrole ring. The peak at 2847 cm^{-1} corresponds to the CH stretching vibration. The peak at 1628 cm^{-1} is for the surface adsorbed water molecules of the tricalcium phosphate. The peak at 1453 cm^{-1} is for the CH_2 stretching vibration^{16,19}. The peak at 1359 cm^{-1} is for the CH asymmetric deformation. The peak at 1220 cm^{-1} is for the stretching vibration of PO_4^{3-} . The peak at 914 cm^{-1} corresponds to the C-O-C stretching vibration. The vibrational peaks due to PO_4^{3-} are seen in the range of 561 - 607 cm^{-1} .

3.2 X-ray Diffraction Analysis (XRD)

The average crystallite size and average crystallinity index of the composites were calculated using Scherrer's formulae. The XRD spectra for cellulose/AA/ β -TCP, cellulose/CA/ β -TCP, cellulose/PVA/ β -TCP, cellulose/PVP/ β -TCP and β -TCP are shown in Fig 2. The distinctive peaks of AA, CA, PVA, and PVP appear in the diffraction patterns of the Cellulose/AA/ β -TCP, Cellulose/CA/ β -TCP, Cellulose/PVA/ β -TCP and Cellulose/PVP/ β -TCP composites after blending with cellulose and β -TCP^{18,21}. When cellulose interacted substantially with the hydroxyl groups of Agar-Agar, Carragenan, PVA, and PVP, the percentage crystallinity of the composites increased^{18,21}. The intensity of the peaks corresponding to the blend composites Cellulose/AA/ β -TCP, Cellulose/CA/ β -TCP, Cellulose/PVA/ β -TCP and Cellulose/PVP/ β -TCP are significantly lowered due to the enhanced diffraction of ceramic crystals or perhaps because the diffraction peaks of β -TCP overlap.

For the blend composite with β -TCP included, a reduced percentage of crystallinity is seen at 42%. The composites show two small, low-intensity 2θ peaks. The diffraction formed around the $2\theta = 22.6, 22.05, 22.57, 22.08$ representing the crystallographic planes of [111], [002] and [040] are in agreement with the JCPDS#030289 value of native cellulose²².

The Crystallinity index (CI) and Average crystallite size (D) values of the samples are listed in Table 1. Accordingly, Cellulose/PVP/ β -TCP composite shows low crystallinity index which may be due to its amorphous nature.

3.3 Thermal Analysis

To assess the thermal stability and comprehend the phase changes of the prepared samples, thermogravimetric (TG) and derivative thermogravimetric (DTG) studies were performed between 5 °C and 600 °C.

3.3 (a) Thermogravimetric analysis

The TGA thermograms for cellulose/AA/ β -TCP, Cellulose/CA/ β -TCP, Cellulose/PVA/ β -TCP and cellulose/PVP/ β -TCP are shown in fig III. For β -TCP, the first weight loss was observed at 250 °C – 350 °C^{20,23}. The stability of β -TCP powders is proved by the lack of weight change after 600 °C. For cellulose/AA/ β -TCP composite, the initial weight loss occurred up to 200 °C which is for the surface absorbed water molecules being about 45%.

The second weight loss was seen at 270 °C – 470 °C which corresponds to Agar-Agar and cellulose at 38%. The third weight loss was at 630 °C proving the decomposition of β -TCP which being about 13%. In cellulose/CA/ β -TCP composite, the initial weight loss occurred at 90 °C is for the organic moiety and surface absorbed water molecule was about 35%. The second weight loss occurred at 1700 °C – 450 °C is for the *I*-carrageenan and cellulose with 42.94%. The third weight loss occurred at 500 °C which is for the decomposition of β -TCP with 13.49%.

In cellulose/PVA/ β -TCP composite, the first weight loss occurred at 150°C which is for the organic moiety and surface absorbed water molecules. The second weight loss occurred at 350°C which is for the decomposition of PVA. The weight loss observed at 470 °C is for the decomposition of cellulose^{19,20}. For cellulose/PVP/ β -TCP composite, the initial weight loss occurred at 100 °C which is for the evaporation of water molecules and organic moiety. The second weight loss occurred between 210 °C – 450 °C which corresponds to the decomposition of cellulose. The third weight loss occurred at 440 °C - 550°C shows the decomposition of PVP. The fourth weight loss happened at 570°C showing the decomposition of β -TCP^{21,22}.

3.3 (b) Differential thermal analysis

DTA thermograms recorded are presented in Fig 4. For β -TCP, the initial endothermic zone ranges from 90°C to 295°C, with a peak at 250°C, corresponding to the dehydration of the precipitating complex and the loss of physically adsorbed water molecules in the hydroxyapatite powder. For Composites Cellulose/AA/ β -TCP, a sharp exothermic peak was observed at 200°C. The loss of hydroxide from the cellulose and agar composite material is the cause of the release of heat by the sample during exothermic operations^{18,19}. The results showed that the composites are thermally stable. For cellulose/CA/ β -TCP composite also an exothermic peak was observed at 160°C, showing the released of heat by the sample during exothermic processes because of the loss of hydroxide from the cellulose and agar composite substance.

The thermal data shows that the composites are thermally stable for fabrication of bio composites materials for biomedical applications.

3.4 UTM analysis

The study of the mechanical properties of β -TCP composites and the correlation between the results have been discussed in UTM analysis. The mechanical responses to tension and strain in the separate β -TCP and cellulose based composites are normal^{13,14}. The tensile strength of each polymer mixture was found to be significantly higher for thin film preparation.

It is evident from the table and Fig.5 that the cellulose/PVA/ β -TCP composite exhibits greater elongation. The tensile characteristics of the combination materials were considerably better, as indicated in Table 3^{14,15}. It has also been suggested that incorporating bioceramics into polymer matrices enhances mechanical properties by creating potent interfacial contacts between the polymer strands and the surface of the bioceramics.

3.5 HR-SEM analysis

The scanning electron microscope is the most sophisticated tool for determining the minute details of the materials' microstructures^{16,17}. To accurately portray the object's surface characteristics in relation to the sample's dimensions, SEM performs point-to-point scanning of the solid surface. The SEM images for β -TCP and β -TCP integrated cellulose based composites are shown in Fig 6.

The SEM images of β -TCP showed the rough outer surface which is due to the chemical treatment. For the composites cellulose/AA/ β -TCP, cellulose/CA/ β -TCP, cellulose/PVA/ β -TCP and cellulose/PVP/ β -TCP it is clearly seen that crystal shaped β -TCP particles are well dispersed in the composites and upon successive drying no agglomeration was found^{18,19}.

3.6 Energy Dispersive X-ray Spectroscopy

Using the EDX spectrum, the composition of polymer mixes and bioceramics was examined, and the findings are presented in Table 4 along with the composition's percentages.

Table 4 shows the percentage composition of the elements in the corresponding prepared composites.

3.7 Biomedical Evaluation

The use of morphologically regulated nanoparticles was crucial in adjustable antibacterial properties^{24,25}. The creation of complex-shaped nanostructures with exact sizes is therefore

gaining popularity. It is well known that when bioceramic nanoparticles are embedded in a polymer matrix, they have a controlled and long-lasting discharge of particles in solution.

3.7.1 Antibacterial study

The results of the antibacterial studies obtained for four human pathogens against Cellulose/AA/ β -TCP, Cellulose/CA/ β -TCP, Cellulose/PVA/ β -TCP, Cellulose/PVP/ β -TCP prepared composites are given in Figs. 7 – 10.

3.7.1 (a) Antibacterial activity of cellulose/AA/ β -TCP

The antibacterial activity of Cellulose/AA/ β -TCP is shown in Fig 7.

From the zone of inhibition, it is observed that cellulose/AA/ β -TCP composite is effective against *Enterococcus fecalis*, *Escherichia coli* and *Staphylococcus aureus*. Their Zone of inhibition values are in close agreement with the positive control.

3.7.1 (b) Antibacterial activity of cellulose/CA/ β -TCP

The antibacterial activity of Cellulose/CA/ β -TCP is shown in Fig 8.

From the zone of inhibition, it is observed that cellulose/CA/ β -TCP composite is effective against *Enterococcus fecalis*, *Escherichia coli* and *Staphylococcus aureus*. Their Zone of inhibition values are in close agreement with the positive control.

3.7.1 (c) Antibacterial activity of cellulose/PVA/ β -TCP

The antibacterial activity of Cellulose/PVA/ β -TCP is shown in Fig 9.

From the zone of inhibition, it is observed that cellulose/PVA/ β -TCP composite is effective against *Enterococcus fecalis*, *Escherichia coli* and *Staphylococcus aureus*. Their Zone of inhibition values are in close agreement with the positive control.

3.7.1 (d) Antibacterial activity of cellulose/PVP/ β -TCP

The antibacterial activity of Cellulose/PV/ β -TCP is shown in Figure 10.

From the zone of inhibition, it is observed that cellulose/PVP/ β -TCP composite is effective against *Enterococcus fecalis*, *Escherichia coli* and *Staphylococcus aureus*. Their Zone of inhibition values are in close agreement with the positive control.

3.7.2 Antifungal activity

The results of the antifungal studies obtained for fungi against Cellulose/AA/ β -TCP, Cellulose/CA/ β -TCP, Cellulose/PVA/ β -TCP, Cellulose/PVP/ β -TCP prepared composites are given in the figs. 11 - 14 and tables 9 – 12.

3.7.2 (a) Antifungal activity of cellulose/AA/ β -TCP

The antifungal activity of Cellulose/AA/ β -TCP is shown in Fig. 11.

From the zone of inhibition, it is observed that cellulose/AA/ β -TCP composite is effective against *Trichoderma viride*, *Candida albicans*. Their Zone of inhibition values are in close agreement with the positive control.

3.7.2 (b) Antifungal activity of cellulose/CA/ β -TCP

The antibacterial activity of Cellulose/CA/ β -TCP is shown in Fig 12.

From the zone of inhibition, it is observed that cellulose/CA/ β -TCP composite is effective against *Trichoderma viride*, *Candida albicans*, *Rhizopus stolonifera*. Their Zone of inhibition values are in close agreement with the positive control.

3.7.2 (c) Antifungal activity of cellulose/PVA/ β -TCP

The antifungal activity of Cellulose/CA/ β -TCP is shown in Fig. 13

From the zone of inhibition, it is observed that cellulose/PVA/ β -TCP composite is effective against *Trichoderma viride*, *Candida albicans*. Their Zone of inhibition values are in close agreement with the positive control.

3.7.2 (d) Antifungal activity of cellulose/PVP/ β -TCP

The antifungal activity of Cellulose/PVP/ β -TCP is shown in Fig. 14.

From the zone of inhibition, it is observed that cellulose/PVA/ β -TCP composite is effective against *Trichoderma viride*, *Candida albicans*. Their Zone of inhibition values are in close agreement with the positive control.

3.7.3 Anticancer Activity

The anticancer activities of all the four composites were performed by MCF 7 cell lines. Measurements were performed and the concentration required for a 50% inhibition (IC_{50}) was determined graphically²². The percentage cell viability was calculated using the formulae,

$$\% \text{ Cell viability} = \text{A570 of treated cells} / \text{A570 of control cells} \times 100$$

The cell viability percentage of the composites cellulose/AA/ β -TCP, cellulose/CA/ β -TCP, cellulose/PVA/ β -TCP and cellulose/PVP/ β -TCP are listed in Fig. 15

The above bar graph shows the anticancer activities of Cellulose/AA/ β -TCP, Cellulose/CA/ β -TCP, Cellulose/PVA/ β -TCP and Cellulose/PVP/ β -TCP composites. It clearly indicates that the cell viability % increases on decrease in concentration. From the comparative bar graph representation, Cellulose/PVA/ β -TCP composites showed better activity than the other composites.

3.7.4 *In vitro* Wound healing

The wound healing test was performed using VERO cell types. The cells were inoculated into six-well dishes and left to incubate for 24 hours. After incubation, the cells were examined for development and a test was performed. Weighed samples were dissolved in DMSO^{23,24}. A sample of 100g/ml was collected for examination. The medium was removed, and the dish was examined under a microscope. A sterile tip was used to make the incision. The well was filled with the appropriate quantity (100g/ml) and incubated. The dish was examined for cell development after 24 hours of incubation (Fig.16).

The wound closure percentage of the composites are listed below in the Table 13.

On comparing the wound closure percentage of the composites, Cellulose/PVA/ β -TCP composite better activity than the other composites. The wound closure % was measured as 46.30%.

4 Conclusion

In this investigation cellulose/ β -TCP based triblock composites were successfully prepared. The composites were characterized by FTIR, XRD and thermal analysis. The microstructure of polymer composites films was studied by SEM. The antimicrobial results showed that

these composites have optimal biomedical applications. The addition of filler significantly enhances the zone of inhibition in antibacterial and antifungal activities when compared to cellulose. Further it was observed that β -TCP composites have comparatively higher wound healing activity than the cellulose. Hence, the composites have vital applications in the medicinal field.

Acknowledgement

We would like to thank the Dr. Amirthavalli Raghupathy Memorial Fund for funding for our research laboratory.

Figures:

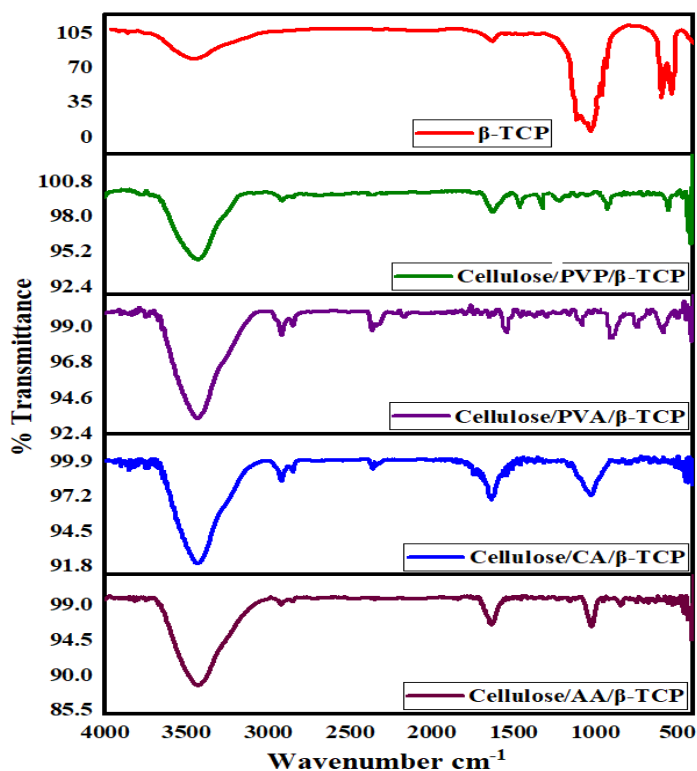


Fig. 1 FTIR spectra β -TCP and β -TCP integrated cellulose-based composites

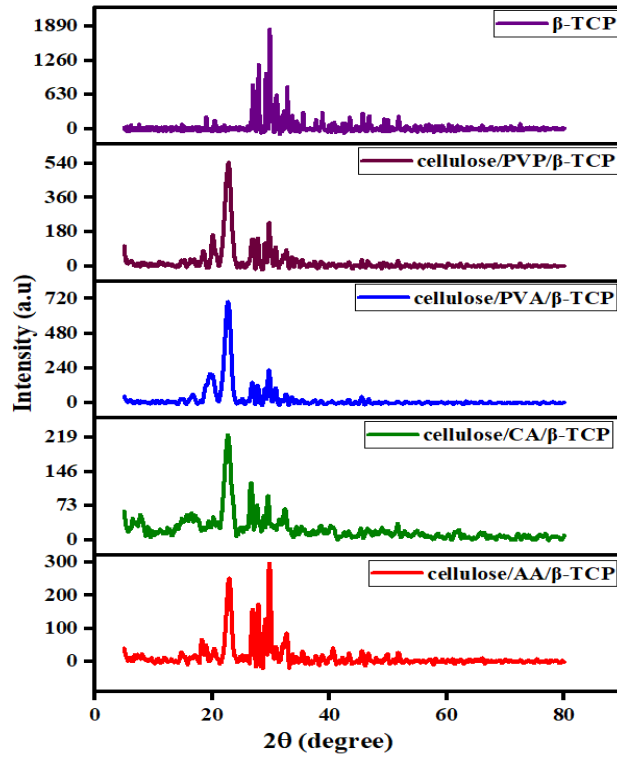


Fig. 2 XRD spectra β -TCP and β -TCP integrated cellulose based composites

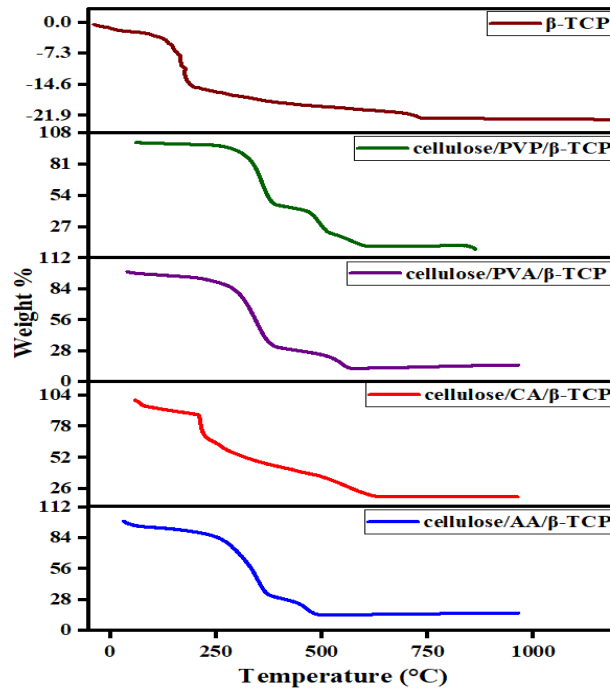


Fig. 3 TGA thermograms for β -TCP and β -TCP integrated cellulose based composites

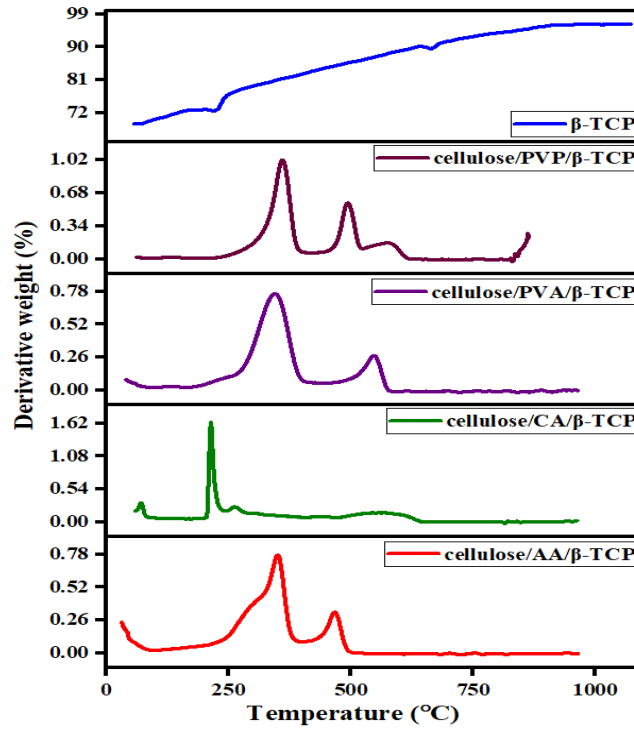


Fig. 4 DTA thermograms for β -TCP and β -TCP integrated cellulose based composites

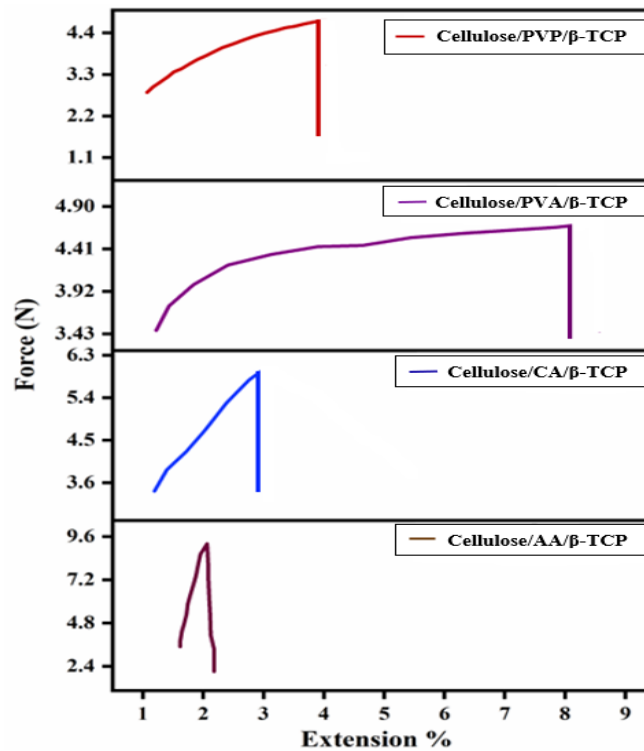


Fig. 5 UTM analysis β -TCP integrated cellulose based composites

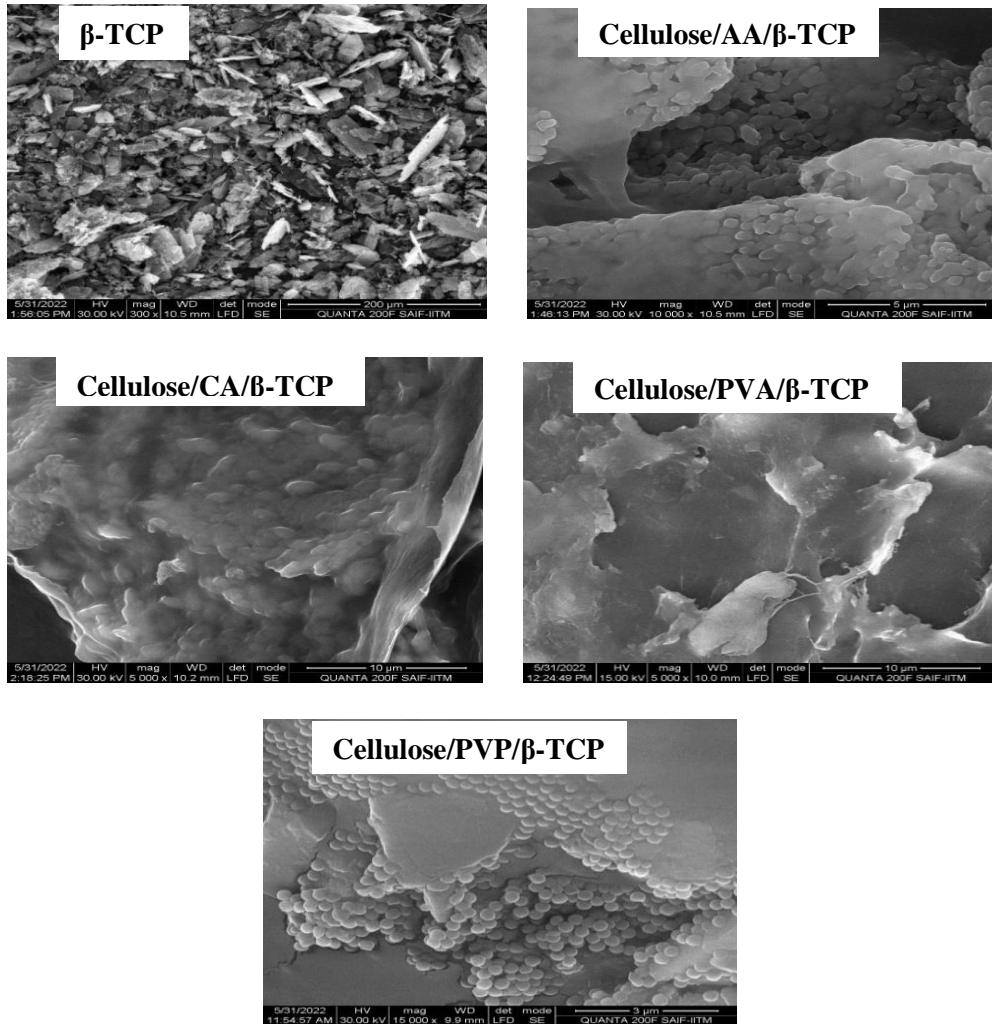


Fig. 6 SEM images of β -TCP and β -TCP integrated cellulose based composites

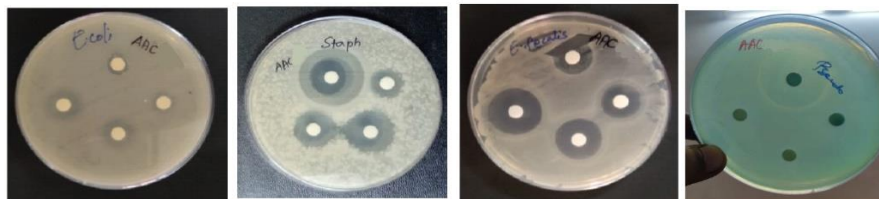


Fig.7 Antibacterial activity for cellulose/AA/ β -TCP



Fig. 8 Antibacterial activity for cellulose/CA/ β -TCP



Fig. 9 Antibacterial activity for cellulose/PVA/β-TCP

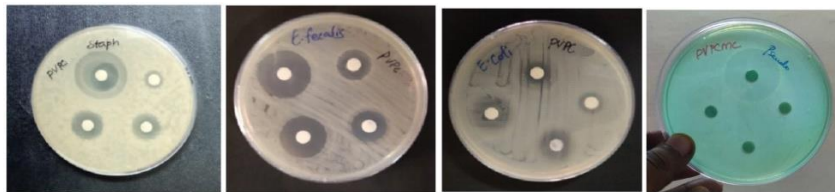


Fig. 10 Antibacterial activity for cellulose/PVP/β-TCP



Fig 11 Antifungal activity for cellulose/AA/β-TCP



Fig. 12 Antifungal activity for cellulose/CA/β-TCP



Fig. 13 Antifungal activity for cellulose/PVA/β-TCP

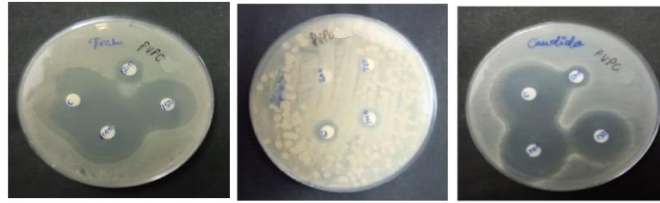


Fig. 14 Antifungal activity for cellulose/PVP/β-TCP

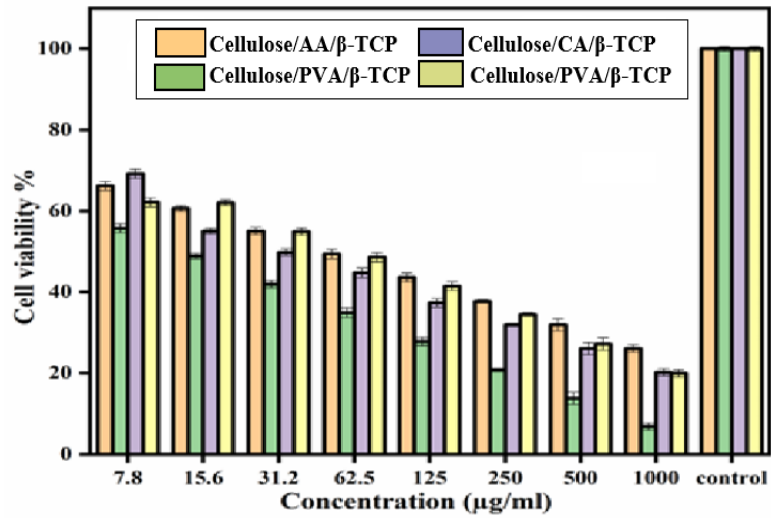


Fig. 15 Comparative cell viability % of composites

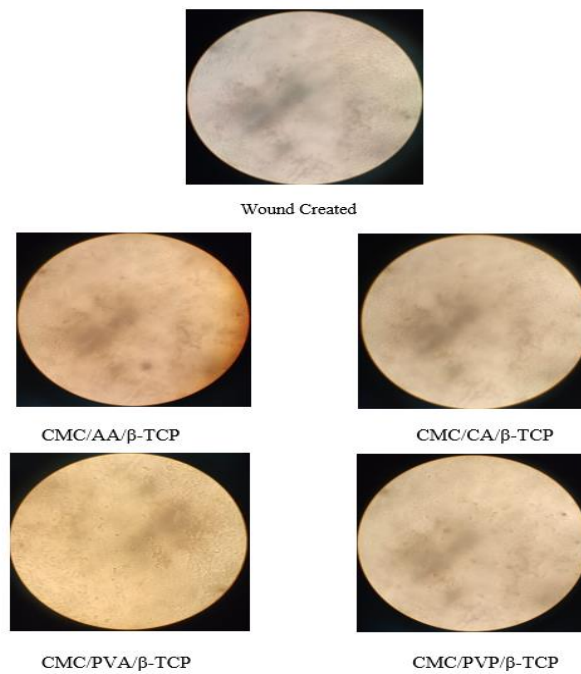


Fig. 16 Wound Healing images of β-TCP integrated cellulose based composites

Table 1 Average crystallite size, Crystallinity index, 2θ values for β -TCP and prepared Composites.

S.No	Composites	Average Crystallite Size	Crystallinity index
1	TCP	18.2nm	51.7%
2	Cellulose/AA/ β -TCP	17.95 nm	46%
3	Cellulose/CA/ β -TCP	16.58 nm	41.78
4	Cellulose/PVA/ β -TCP	15.03 nm	40.5%
5	Cellulose/PVP/ β -TCP	14.02 nm	36.15%

Table 2 Melting temperature (T_m) and decomposition temperature (T_d) for β -TCP and prepared composites

S.No	Composites	T_m ($^{\circ}$ C)	T_d ($^{\circ}$ C)
1.	Cellulose/AA/ β -TCP	103 $^{\circ}$ C	628 $^{\circ}$ C
2.	Cellulose/CA/ β -TCP	147 $^{\circ}$ C	742 $^{\circ}$ C
3.	Cellulose/PVA/ β -TCP	160 $^{\circ}$ C	572 $^{\circ}$ C
4.	Cellulose/PVP/ β -TCP	162 $^{\circ}$ C	532 $^{\circ}$ C
5.	β -TCP		730 $^{\circ}$ C

Table 3 Maximum load, Tensile strength Elongation at break, Extension at maximum load, Thickness and Area of the Polymer composites.

S. No	Polymer nano composites	Maximum Load (N)	Tensile strength (MPa)	Elongation at break (%)	Extension at maximum load (mm)	Thickness (mm)	Area (mm)
1.	Cellulose/AA/ β -TCP	31.57	27.27	1.67	0.50	0.11	1.3
2.	Cellulose/CA/ β -TCP	35.84	17.36	3.50	1.05	0.22	2.1
3.	Cellulose/PVA/ β -TCP	12.54	12.77	16.33	4.90	0.12	1.2
4.	Cellulose/PVP/ β -TCP	8.95	1.57	2.00	0.60	0.55	5.6

Table 4 EDX spectra of β -TCP, Cellulose/AA/ β -TCP, Cellulose/CA/ β -TCP, Cellulose/PVA/ β -TCP, Cellulose/PVP/ β -TCP

Composites	Elements	Weight Percentage (%)	Atomic Percentage (%)
β-TCP	<i>C</i>	23.19	38.36
	<i>O</i>	27.84	35.05
	<i>P</i>	17.47	13.04
	<i>Ca</i>	33.68	15.55
Cellulose/AA/β-TCP	<i>C</i>	47.75	57.04
	<i>O</i>	36.66	34.91
	<i>P</i>	03.03	02.01
	<i>S</i>	07.76	03.19
	<i>Ca</i>	04.72	02.62
Cellulose/CA/β-TCP	<i>C</i>	46.18	56.71
	<i>O</i>	34.70	34.28
	<i>P</i>	03.53	02.01
	<i>S</i>	07.72	05.17
	<i>Ca</i>	05.28	02.64
Cellulose/PVA/β-TCP	<i>C</i>	37.23	53.74
	<i>O</i>	28.62	28.74
	<i>P</i>	07.05	04.37
	<i>S</i>	09.70	05.67
	<i>Ca</i>	13.85	06.55
Cellulose/PVP/β-TCP	<i>C</i>	32.23	47.70
	<i>O</i>	16.58	16.15
	<i>P</i>	04.78	03.73
	<i>S</i>	10.16	06.63
	<i>Ca</i>	11.63	03.23

Table 5 Antibacterial activity of cellulose/AA/ β -TCP

Organisms	Zone of Inhibition (mm)			Antibiotic (1mg/ml)
	1000	750	500	
<i>Staphylococcus aureus</i>	18	17	12	20
<i>Escherichia coli</i>	13	11	10	13
<i>Enterococcus fecalis</i>	23	21	15	17
<i>Pseudomonas aeruginosa</i>	1	1	1	26

Table 6 Antibacterial activity of Cellulose/CA/ β -TCP

Organisms	Zone of Inhibition (mm)			Antibiotic (1mg/ml)
	1000	750	500	
<i>Staphylococcus aureus</i>	15	15	11	17
<i>Escherichia coli</i>	16	16	13	21
<i>Enterococcus fecalis</i>	20	18	15	15
<i>Pseudomonas aeruginosa</i>	2	1	1	25

Table 7 Antibacterial activity of Cellulose/PVA/ β -TCP

Organisms	Zone of Inhibition (mm)			Antibiotic (1mg/ml)
	1000	750	500	
<i>Staphylococcus aureus</i>	15	13	7	18
<i>Escherichia coli</i>	18	15	13	20
<i>Enterococcus fecalis</i>	20	20	15	15
<i>Pseudomonas aeruginosa</i>	1	1	1	24

Table 8 Antibacterial activity of Cellulose/PVP/ β -TCP

Organisms	Zone of Inhibition (mm)			Antibiotic (1mg/ml)
	1000	750	500	
<i>Staphylococcus aureus</i>	16	14	9	19
<i>Escherichia coli</i>	17	15	13	19
<i>Enterococcus fecalis</i>	24	21	17	17
<i>Pseudomonas aeruginosa</i>	1	1	1	27

Table 9 Antifungal activity of cellulose/AA/ β -TCP

Organisms	Zone of Inhibition (mm)			Antibiotic (1mg/ml)
	Sample (μ g/ml)			
	1000	750	500	
<i>Trichoderma viride</i>	40	31	21	37
<i>Rhizopus sp.</i>	11	09	1	10
<i>Candida albicans</i>	35	13	11	37

Table 10 Antifungal activity of cellulose/CA/ β -TCP

Organisms	Zone of Inhibition (mm)			Antibiotic (1mg/ml)
	Sample (μ g/ml)			
	1000	750	500	
<i>Trichoderma viride</i>	33	27	26	40
<i>Rhizopus sp.</i>	12	06	1	14
<i>Candida albicans</i>	33	23	12	24

Table 11 Antifungal activity of Cellulose/PVA/ β -TCP

Organisms	Zone of Inhibition (mm)			Antibiotic (1mg/ml)
	Sample (μ g/ml)			
	1000	750	500	
<i>Trichoderma viride</i>	31	20	08	33
<i>Rhizopus sp.</i>	10	07	1	13
<i>Candida albicans</i>	30	20	13	30

Table 12 Antifungal activity of cellulose/PVP/ β -TCP

Organisms	Zone of Inhibition (mm)			Antibiotic (1mg/ml)
	Sample (μ g/ml)			
	1000	750	500	
<i>Trichoderma viride</i>	33	25	14	37
<i>Rhizopus sp.</i>	09	1	1	11
<i>Candida albicans</i>	31	26	13	34

Table 13 Wound closure % of the composites

S.No	Composites	Wound created (before)	After	Wound closure %
1.	Cellulose/AA/ β -TCP	5.16mm	3.16mm	35.8%
2.	Cellulose/CA/ β -TCP	5.16mm	3.29mm	41.02%
3.	Cellulose/PVA/ β -TCP	5.16mm	2.42mm	46.30%
4.	Cellulose/PVP/ β -TCP	5.16mm	2.73mm	41.73%

References

1. T. P. Sathishkumar, L. Rajeshkumar, G. Rajeshkumar, M. R. Sanjay, S. Siengchin , N.Thakrishnan , E3S Web of Confe. 355, 02006, 2022.
2. P. Madhu, M. R. Sanjay P., Senthamaraikannan , S. Pradeep, S. S. Saravanakumar, B.Yogesha, J Nat Fibers. 16, 1132, 2018.
3. T. Rohan,B. Tushar, G.,T. Mahesha, IOP Conf Series Mater Sci Eng. 314, 012020, 2018.
4. T.Y.Gowda, M. R. Sanjay, K.S. Bhat, P.Madhu ,P. Senthamaraikannan, B.Yogesha, Cogent Eng. 5, 1446667, 2018.
5. B. T. Narendiranath, S.S.Aravind , Kumar KSN, Rao MSS. Int J Mech Eng Technol. 9, 11, 2018.
6. M. R. Sanjay, G. R.Arptha, L .L. Naik, K. Gopalakrishna, B. Yogesha, Nat Resour. 7, 2108, 2016.
7. R.S. Rana, R. Purohit, Mater Today Proc. 4, 3466, 2017.
8. Y. Swolfs, L. Gorbatikh , I. Verpoest Appl Sci Manuf. 67, 181, 2014.
9. M.T. Hayajneh, M.M.Al-Shrida, F.M.AL-Oqla, e-Polymers., 22, 641, 2022
10. V. Dhawan, S. Singh, I. Singh, J Compos. 7, 792620, 2013.
11. E. Habib, R. Wang, Y.Wang, M. Zhu , X.X. Zhu. ACS Biomater Sci Eng. 2, 1, 2016.
12. M. T. Hayajneh, F.M. AL-Oqla, M .M. Al-Shrida, e-Polymers. 21, 710, 2021.
13. M. Ramesh, L .Rajeshkumar, V. Bhuvaneshwari, Emergent Mater. 5, 833, 2021.
14. D. Balaji, M. Ramesh, T. Kannan, S. Deepan V., Bhuvaneshwari, L.Rajeshkumar Mater Today Proc. 42, 350, 2021.

JOURNAL OF ISAS VOLUME 2, ISSUE 2, OCTOBER 2023

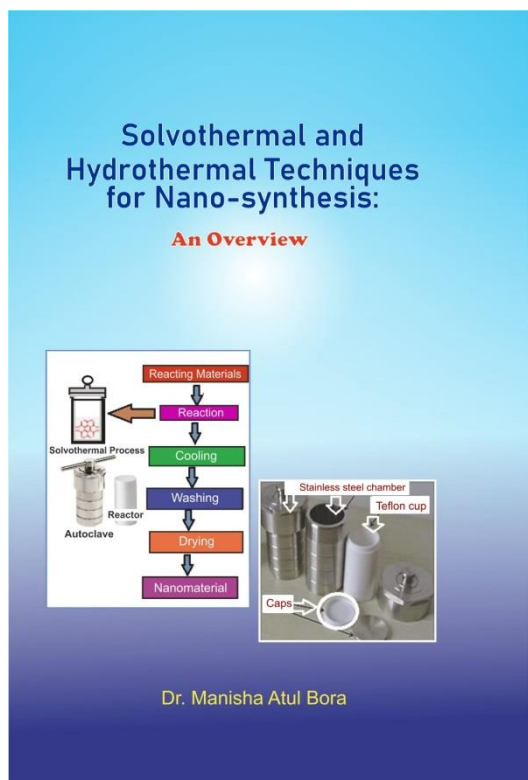
15. de Araujo Alves Lima R, Kawasaki Cavalcanti D, de Souza e Silva Neto J, Meneses da Costa H, Banea MD. Polym Compos. 41, 314, 2020.
16. S. B. R.Devireddy, S.Biswas , Polym Compos. 38, 1396, 2017
17. Salama, International Journal of Biological Macromolecules, 127, 606, 2019
18. A. Allwyn Sundar Raj, T.V. Ranganathan, J. of Pharmacy Res., 9, 4309, 2018.
19. T.S. Kiruthika, E.K.T. Sivakumar, V. Jaisankar, Asian J. of Chem., 34, 2022, 2843.
20. H. Chaair, H. Labjar, O. Britel, Synthesis of β -tricalcium phosphate, Morphologie, 313, 2017.
21. M. Sasikala,, and M. J. Umapathy, New Journal of Chemistry, 42.24, 19979, 2018.
22. Kumar, Anuj, Y. S. Negi, N. K. Bhardwaj, and V. Choudhary, Advanced Materials Letters, 4.8, 626, 2013
23. Liu, Liying, Rui Cai, Yejing Wang, Gang Tao, Lisha Ai, Peng Wang, and others, International Journal of Molecular Sciences, 19.10, 2018.
24. S. Maheshwari, K.Uma, M. Govindan, A. Raja,.M. Raja, B.S. Pravin, and S. Vasanth Kumar, Bio-Medical Materials and Engineering, 28.4, 401, 2017.
25. M. Hiljanen-Vainio, M.Heino , J.V. Sepp.al. Polymer, 39, 865, 1998.

Review of the Booklet: “Solvothermal and Hydrothermal Techniques for Nano-synthesis: An Overview by Dr. Manisha Bora

Dr. Dinesh Amalnerkar

Professor Emeritus, Technology Department, Savitribai Phule Pune University, Pune 411007

dpa54@yahoo.co.in



Dr. Manisha Bora has come with handy booklet on “*Solvothermal and Hydrothermal Techniques for Nano-synthesis*” in the same timeframe of October 2023 when Nobel prize in Chemistry has been awarded to three American Professors Bawendi, Brus and Yekimov for their pioneering research on Q-Dots, the tiniest components of nanotechnology. What a great coincidence! This booklet is thus a timely and welcome addition in the sphere of nanotechnology. It comprises in all 12 chapters followed by apt

references at the end. Illustrative figures and synthesis equations are provided at appropriate places. Table-1 furnishes summary of hydrothermal and solvothermal reaction conditions for the synthesis of typical nanomaterials and their focussed end-applications. It is well-established that hydrothermal/solvothermal synthesis conditions lead to formation of nanostructures with complex morphological features/ hierarchical nano- architecture which, in turn, can enhance the utility of the envisaged end-application. Perhaps, inclusion of representative FESEM and FETEM images in this booklet could have been very useful for clarity on nano-scale formation and also to prove the merits of hydrothermal/solvothermal

JOURNAL OF ISAS VOLUME 2, ISSUE 2, OCTOBER 2023

techniques over other techniques. I sometime tend to refer hydrothermal/solvothermal reactor as ‘house-hold pressure cooker’ and when combined with the usage of microwave oven for ultra-fast heating, the pressure-cooker+microwave combination can generate useful ‘kitchen-chemistry’ with interesting novel applications. Dr.Manisha has briefly touched upon this aspect also in this endeavour. In nutshell, the novice as well as seasoned researches in the domain of nanotechnology can find this booklet quite beneficial.

The booklet is a recent publication (6.10.2023) by ISAS, Pune Chapter and is a low priced (Rs 50/-) , easily affordable and may be purchased from: :

Dr. Nilima S. Rajurkar,

Chairperson, Pune Chapter.

nilima@rediffmail.com